Check for updates

Nanoparticle-encapsulated siRNAs for gene silencing in the haematopoietic stem-cell niche

Marvin Krohn-Grimberghe[1,2,8], Michael J. Mitchell [ID][3,4,8], Maximilian J. Schloss[1,8], Omar F. Khan [ID][3], Gabriel Courties[1], Pedro P. G. Guimaraes[3], David Rohde[1], Sebastian Cremer[1], Piotr S. Kowalski [ID][3], Yuan Sun[1], Mingchee Tan[3], Jamie Webster[3], Karin Wang [ID][5], Yoshiko Iwamoto[1], Stephen P. Schmidt[1], Gregory R. Wojtkiewicz [ID][1], Ribhu Nayar[1], Vanessa Frodermann [ID][1], Maarten Hulsmans [ID][1], Amanda Chung[5], Friedrich Felix Hoyer[1], Filip K. Swirski [ID][1], Robert Langer [ID][3], Daniel G. Anderson [ID][3,8] ✉ and Matthias Nahrendorf [ID][1,6,7,8] ✉

Bone-marrow endothelial cells in the haematopoietic stem-cell niche form a network of blood vessels that regulates blood-cell traffic as well as the maintenance and function of haematopoietic stem and progenitor cells. Here, we report the design and in vivo performance of systemically injected lipid–polymer nanoparticles encapsulating small interfering RNA (siRNA), for the silencing of genes in bone-marrow endothelial cells. In mice, nanoparticles encapsulating siRNA sequences targeting the proteins stromal-derived factor 1 (Sdf1) or monocyte chemotactic protein 1 (Mcp1) enhanced (when silencing *Sdf1*) or inhibited (when silencing *Mcp1*) the release of stem and progenitor cells and of leukocytes from the bone marrow. In a mouse model of myocardial infarction, nanoparticle-mediated inhibition of cell release from the haematopoietic niche via *Mcp1* silencing reduced leukocytes in the diseased heart, improved healing after infarction and attenuated heart failure. Nanoparticle-mediated RNA interference in the haematopoietic niche could be used to investigate haematopoietic processes for therapeutic applications in cancer, infection and cardiovascular disease.

Human bone marrow harbours about 10,000 bona fide haematopoietic stem cells as well as millions of downstream progenitors and releases billions of blood cells into the circulation every day[1,2]. The organ produces a cellular ensemble that accomplishes vital tasks including oxygen transport, defence against pathogens and clotting[1,3]. The activities of its inhabitants, such as cell quiescence, proliferation, differentiation and migration, are adjusted to current systemic needs and regulated by non-haematopoietic bone marrow niche cells[3,4]. This cast of supporting cells includes endothelial cells, which instruct haematopoietic cell behaviour via a mix of soluble and cell-surface-bound signals[1,2,5,6]. Niche cells receive circulating and neuronal signals from outside the marrow and relay them to haematopoietic stem and progenitor cells (HSPCs)[7].

Over the past decade, many niche cell steady-state functions have been discovered, leading to approved drugs for stem-cell mobilization before transplantation[8]. Drugs such as filgrastim that disrupt the interactions between stromal-derived factor 1 (SDF1) and its receptor CXCR4 on leukocytes and HSPCs are now widely utilized as agents to mobilize stem cells into the bloodstream for bone marrow transplantation[9]. Such agents have primarily been applied in the realm of haematology/oncology; however, recent evidence suggests that leukocyte and HSPC release from bone marrow plays an essential role in many other chronic inflammatory conditions, including

cardiovascular disease[10]. Broadly speaking, the number of circulating leukocytes and the production of blood components in the haematopoietic niche correlate closely with mortality[10], and if the bone marrow fails altogether, the organism succumbs within a week or two[11,12]. Therefore, technologies that modulate cell behaviour within the haematopoietic niche could improve our fundamental understanding and treatment of a range of disease processes that are governed by bone-marrow-derived leukocytes.

RNA interference (RNAi) therapeutics are a potentially attractive means to influence protein expression within the haematopoietic niche, as they can be used to silence nearly any gene within the body to achieve therapeutic effects[13]. Currently, the most advanced RNAi therapeutic is patisiran, a small interfering RNA (siRNA) lipid nanoparticle-based drug[14]. Patisiran, recently approved by the FDA, inhibits hepatic transthyretin production as a form of transthyretin amyloidosis therapy[14]. Because the gene sequences are known, siRNA drugs can be screened for in silico, produced and validated within very short time spans. However, although potent siRNAs can be rapidly identified, systemic delivery to the appropriate tissue can prove challenging. The use of RNAi to treat disease requires effective methods of targeted delivery, as 'naked' siRNAs are unstable in the bloodstream and do not readily traverse cell membranes[13].

With significant advantages over their non-formulated and free drug counterparts, nanoparticle delivery systems have been
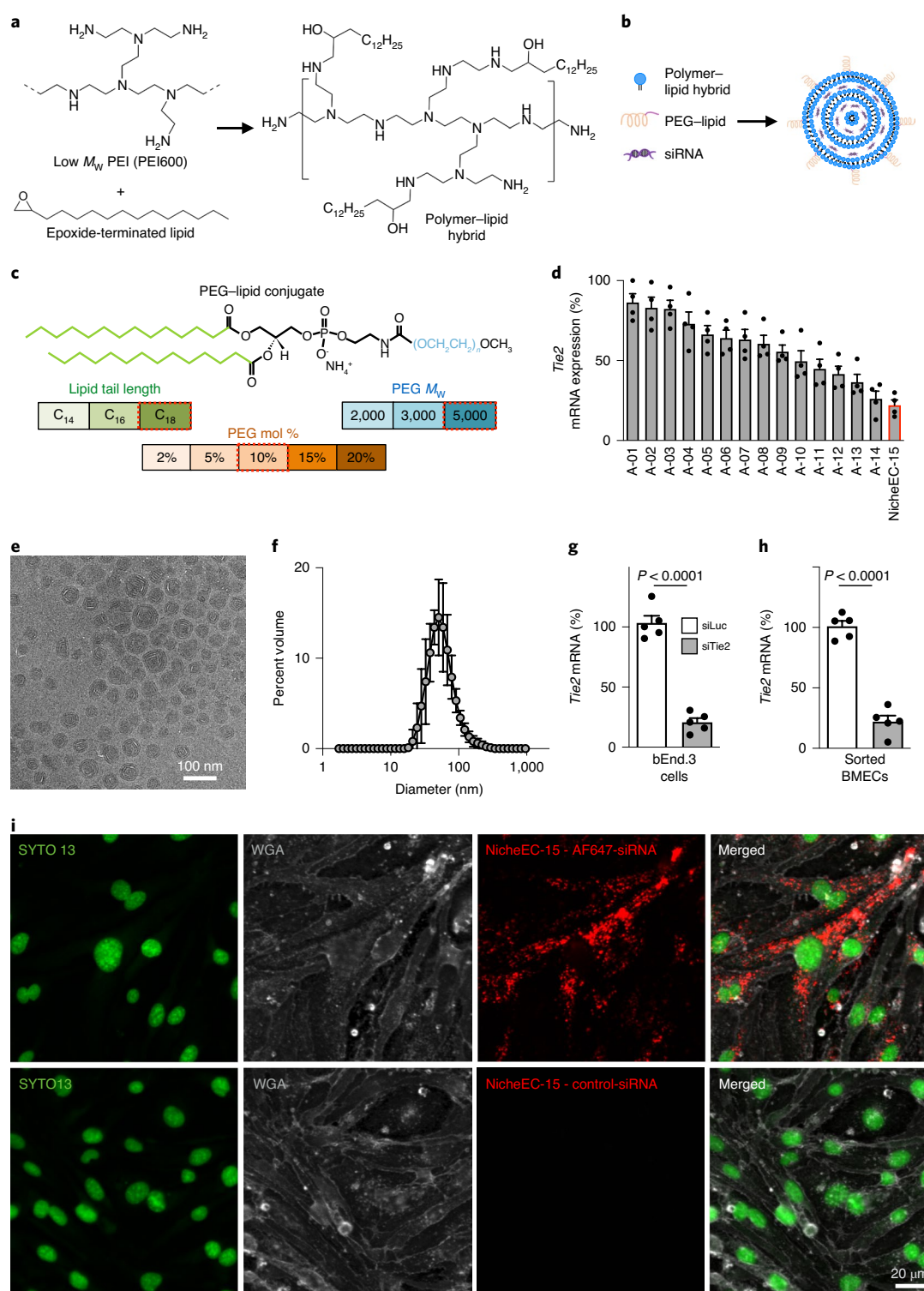
Fig. 1 | Composing a BMEC-targeting nanoparticle. a, Synthesis scheme of the epoxide-modified polymer–lipid hybrid material. **b**, Nanoparticles consisting of lipid hybrid, siRNA and a PEG–lipid conjugate were synthesized via microfluidic mixing. **c**, PEG–lipid conjugate parameters were varied to form a library of unique nanoparticles for siRNA delivery to BMECs. Values outlined by red dashed boxes indicate the best silencing efficiency. **d**, *Tie2* silencing in femoral bone marrow of C57BL/6 mice 48 h after injection of each nanoparticle containing siRNA against *Tie2* (dosage, 1.0 mg kg^{-1}; $n = 4$ mice per group; data are normalized to mRNA expression in naive mice). The strongest silencing was seen for NicheEC-15 nanoparticles (highlighted in red). **e**, Cryo-transmission electron microscopy (TEM) of NicheEC-15 nanoparticles. **f**, Hydrodynamic diameter of NicheEC-15 nanoparticles. **g,h**, *Tie2* silencing in bEnd.3 (**g**) and sorted BMECs (**h**) 24 h after addition of siLuc or siTie2 to the culture medium. *Tie2* mRNA expression after exposure to siLuc was normalized to 100% ($n = 3$ independent experiments (**g**) or three mice (**h**) per group; two-sided *t*-test). **i**, Confocal microscopy of bEND.3 cells 2 h after adding NicheEC-15 to the culture medium. Nuclei were stained with SYTO 13 and cell membranes with wheat germ agglutinin (WGA). In the upper panels the nanoparticles were visualized by siRNA labelled with Alexa Fluor 647 (AF647). In the lower panels, an unlabelled control siRNA was used. This experiment was repeated twice with similar results. Data are shown as mean ± s.e.m.

used effectively as delivery vehicles in several medical settings[15]. For siRNA delivery, nanoparticles' key advantages are (1) preventing nucleic acid degradation by serum endonucleases in blood, (2) avoiding renal clearance from the bloodstream, (3) delivering cargo to specific cells by tailoring the nanoparticle surface chemistry and (4) mediating target cell entry and endosomal escape to enable nucleic acid release into the cytoplasm[13,16]. Delivery materials differ in efficiency, toxicity and biodistribution, and certain nanoparticles have avidity to certain cell types, tissues and organs[17], particularly to hepatocytes, leukocytes and endothelial cells[18–24]. Of note, our group previously reported a nanoparticulate formulation consisting of low-molecular-weight polyamines and lipids that mediated potent gene silencing in endothelial cells residing in the lung[19].

Here we describe the development of an siRNA formulation capable of delivering siRNA to endothelial cells in the haematopoietic niche. We first screened a library of nanoparticles based on a class of nanoparticle-forming materials that were generated by combinatorial chemical synthesis and deliver siRNA to lung endothelium in vivo[19,25]. These materials were synthesized by reacting low-molecular-weight polyamines with epoxide-terminated lipids using an epoxide ring-opening reaction[19]. By screening a library of these nanoparticles in vivo, we developed a polymer–lipid hybrid nanoparticle for delivery to bone marrow endothelial cells. In a series of proof-of-concept experiments, we silence endothelial cell expression of two quintessential haematopoietic niche factors, thereby altering HSPC behaviour and systemic leukocyte supply. Such an RNAi approach is of interest to modulating haematopoietic cell activity and abundance in fundamental science and to developing new therapeutics.

Results

Nanoparticle screen for in vivo siRNA delivery to the haematopoietic niche. Bone-marrow endothelial cells (BMECs) are an integral component of the haematopoietic niche and instruct stem cell and leukocyte behaviour. Cell-specific deletion experiments revealed that both progenitor proliferation and migration are governed by BMEC-derived signals[1,2]. Based on previously reported endothelial-cell-avid delivery materials[19], we began developing suitable delivery materials for BMECs. We synthesized a polymer–lipid hybrid material by reacting C15 epoxide-terminated lipids with low-molecular-weight polyamines (PEI600) at a 14:1 molar ratio via Michael addition chemistry (Fig. 1a). The resulting material was combined with siRNA and a polyethylene glycol (PEG)–lipid conju-

gate in a high-throughput microfluidic mixing chamber[26] to formulate nanoparticles via electrostatic interactions between the cationic polymeric material and the negatively charged nucleic acid (Fig. 1b). Using this nanomaterial as a starting point, we then tested different PEG surface coatings that alter the biodistribution and pharmacokinetics of various nanoparticle types[27,28]. We hypothesized that modulating the nanoparticle PEG architecture enhances nanoparticle siRNA delivery to the bone marrow. By altering their PEG decoration, we created a library of 15 nanoparticle formulations, with three key parameters of the PEG–lipid conjugate modified in each candidate nanoparticle: (1) the molecular weight of the PEG surface coating (molecular weight range: 2,000–5,000), (2) PEG surface density, which was altered by varying the overall molar percentage of PEG within the formulation (molar percentage range, 2–20%) and (3) the length of the lipid chain that anchors PEG within the nanoparticle membrane (Fig. 1c). We injected this mini-library intravenously into mice (1.0 mg per kg body weight) and then assessed *Tie2* silencing in the bone marrow. *Tie2* was chosen as a silencing target purely for this delivery and silencing assay, and not for the gene's function, which has roles beyond BMECs. Using a branched DNA assay, we identified the best nanoparticle formulation (termed NicheEC-15), which induced ~80% *Tie2* in vivo gene silencing in bone marrow (Fig. 1d) without disrupting the vascular anatomy (Supplementary Fig. 1). Cryo-scanning electron microscopy and dynamic light scattering (DLS) showed that NicheEC-15 formed multilamellar nanoparticles (Fig. 1e) with a 60–80-nm diameter (Fig. 1f). We next assessed NicheEC-15 for *Tie2* silencing in endothelial cells in vitro. Nanoparticles containing 60 nM *Tie2* siRNA induced potent gene silencing in the mouse endothelial cell line bEnd.3 (Fig. 1g) and in primary murine BMECs (Fig. 1h). Confocal microscopic imaging confirmed efficient in vitro uptake of nanoparticles containing fluorescent siRNA (Fig. 1i).

In vivo behaviour of the lead particle NicheEC-15. The in vivo blood half-life of NicheEC-15 nanoparticles, containing a fluorescent siRNA, was measured to be 13.8 min by fitting the decrease in blood fluorescence intensity over time after a single intravenous (i.v.) injection (Fig. 2a). Using a range of 0.01–1.0 mg kg^{-1} siTie2, we observed dose-dependent knockdown of *Tie2* messenger RNA (mRNA) expression by quantitative polymerase chain reaction (qPCR; Fig. 2b). At a dose of 1 mg kg^{-1} siTie2, the knockdown achieved with NicheEC-15 nanoparticles was ~50% stronger than 7C1 nanoparticles[19], a previously described nanoparticle

Fig. 2 | In vivo uptake of NicheEC-15 nanoparticles in BMECs. a, The decline in blood fluorescence intensity was measured over time following a single injection of NicheEC-15 AF647-siRNA. The in vivo circulation half-life of NicheEC-15 nanoparticles was calculated to be 13.8 min ($n = 5$ mice). **b,** Dose–response curve of *Tie2* silencing in whole bone marrow after in vivo injection of NicheEC-15 or 7C1 nanoparticles encapsulating siTie2 by branched DNA (bDNA) assay (dose range 0.01–1.0 mg kg^{-1}, $n = 4$ mice per group and time point). **c,** Time course of *Tie2* expression in whole bone marrow following a single 1.0 mg kg^{-1} injection of NicheEC-15 or 7C1 encapsulating siTie2 by bDNA assay. Femurs were collected 1–18 days post-injection ($n = 4$ mice per group and time point). The plots in **b** and **c** show fold changes in mRNA expression compared to naive mice. **d,** Intravital microscopy of the skull bone marrow 2 h after injection of NicheEC-15 with AF647-siRNA cargo. The vasculature was stained with PE-labelled CD31 and Sca-1 antibodies and OsteoSense was used to visualize bone. **e,** Mice were euthanized 2 h after i.v. injection of 2 mg kg^{-1} NicheEC-15 AF647-siRNA. BMECs were gated as shown in the FACS plots (left and middle). A histogram of endothelial cells (ECs) is shown (right) with CD45$^+$ leukocytes and endothelial cells of uninjected control mice. SCC indicates side scatter. **f,** ImageStream results of endothelial cells 2 h after injection of NicheEC-15 AF647-siRNA (top) compared to PBS-injected controls (bottom). **g,h,** Uptake of the nanoparticles in endothelial cells compared to control mice injected with PBS. Of 816 endothelial cells, 764 (93.4%) were positive for siAF647 based on mean AF647 positive pixel number (=AF647$^+$ pixel) (**g**) and 682 (83.6%) based on peak cellular signal intensity for AF647 (=AF647 SI) (**h**). **i,** ImageStream results of endothelial cells 2 h after injection of NicheEC-15 AF647-siRNA with additional staining for podoplanin, identifying sinusoidal endothelial cells. **j,** ImageStream results of leukocytes 2 h after injection of NicheEC-15 AF647-siRNA. **k,l,** Uptake of the nanoparticles in endothelial cells compared to leukocytes based on mean AF647 positive pixel number (**k**) and peak cellular signal intensity for AF647 (**l**). WBC indicates CD45$^+$ leukocytes. Experiments **d–l** were repeated twice with similar results. **m,** Mean fluorescence intensity by flow cytometry of uninjected mice, CD45$^+$ leukocytes, BMECs and lung endothelial cells 2 h after injection of 2 mg kg^{-1} AF647-siRNA encapsulated into the 7C1 or NicheEC-15 nanoparticles ($n = 4$ mice each, except CD45$^+$ $n = 8$; one-way analysis of variance (ANOVA) with multiple comparisons). **n,** The mean fluorescence intensity (MFI) of the BMECs was divided by the MFI of lung endothelial cells for 7C1 and NicheEC-15, giving 1.19 for 7C1 and 3.17 for NicheEC-15. **o,** Comparison of *Tie2* silencing in whole bone marrow and lung after in vivo injection of NicheEC-15 or 7C1 encapsulating siTie2 by a bDNA assay (dose 1.0 mg kg^{-1}, $n = 4$ mice each; two-sided *t*-test without multiple comparisons; fold changes in mRNA expression compared to naive mice). Data are shown as mean ± s.e.m.

with excellent silencing in endothelial cells. A single injection of NicheEC-15 nanoparticles containing $1.0\,mg\,kg^{-1}$ siTie2 induced long-lasting knockdown for more than two weeks (Fig. 2c). To better understand the uptake patterns of NicheEC-15 nanoparticles, we next directly visualized the haematopoietic niche using intravital microscopy of the skull bone marrow of mice. The vasculature was stained by intravenously injecting a cocktail of PE-labelled CD31

and Sca-1 antibodies, while OsteoSense, a molecular imaging probe that enriches in osteoblasts, outlined the bone surface surrounding haematopoietic niches[29]. Two hours after injecting NicheEC-15-containing fluorescently tagged siRNA, we primarily found the siRNA associated imaging signal in the bone marrow vasculature (Fig. 2d). The cellular distribution of NicheEC-15 nanoparticles was measured by flow cytometric analysis of the bone marrow. Although
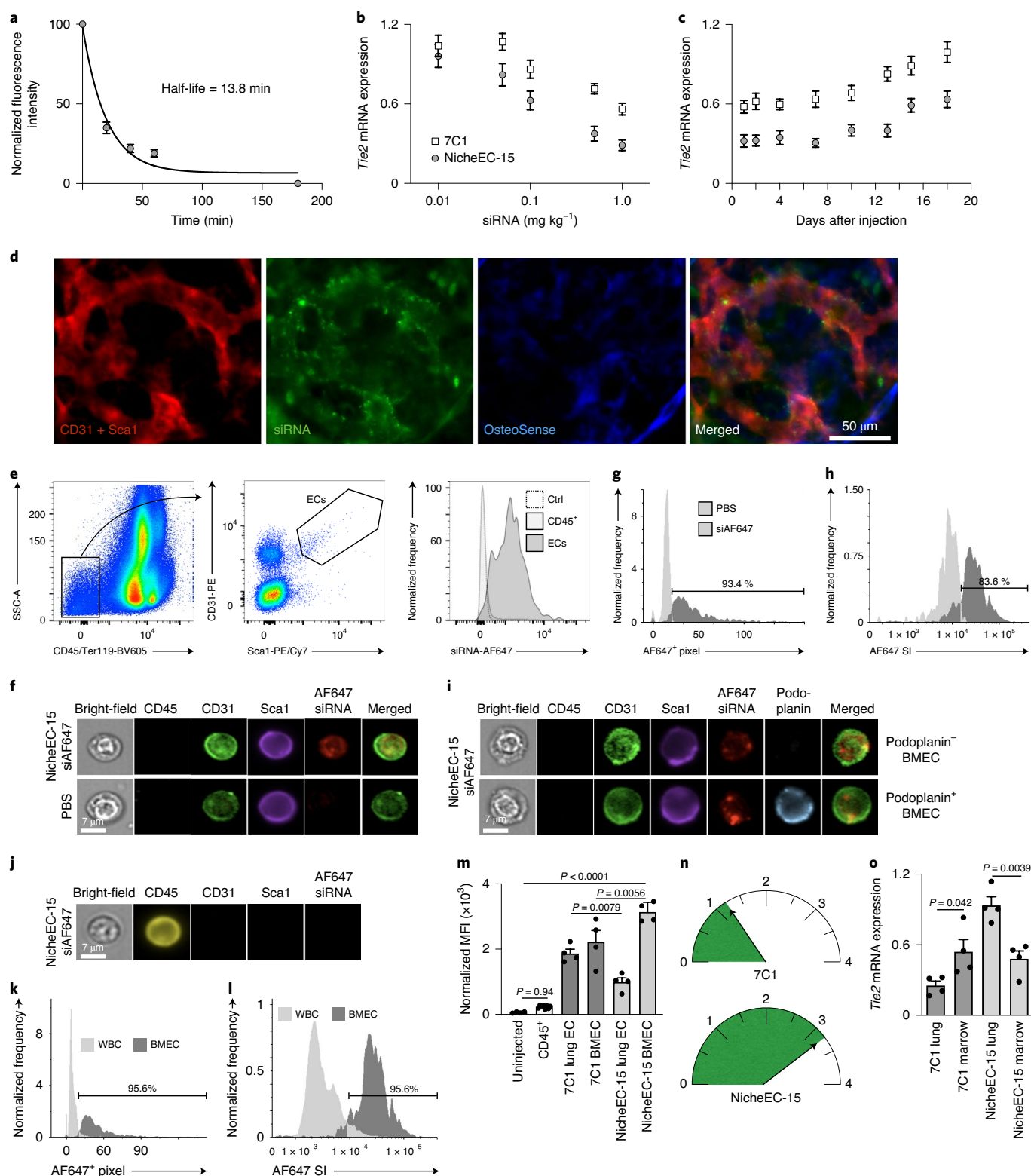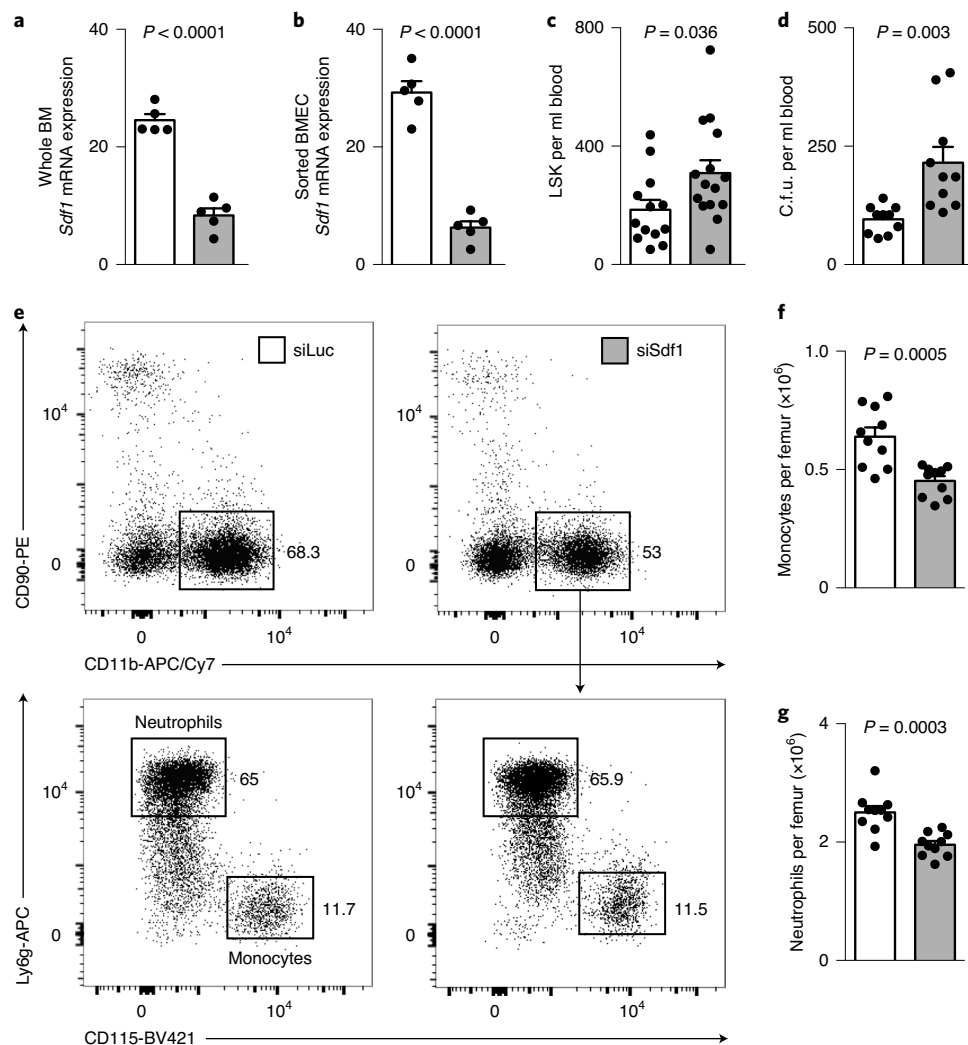
Fig. 3 | Effects of siSdf1 silencing on the bone marrow. a, *Sdf1* expression in whole bone marrow by qPCR ($n = 5$ mice each). Mice were injected with 2 mg kg^{-1} siSdf1 or control siRNA targeting luciferase (siLuc) on day 0 and day 3 and collected on day 5. **b**, qPCR for *Sdf1* in sorted BMECs ($n = 5$ mice each). The results in **a** and **b** have been normalized to GAPDH expression. **c**, Number of blood LSK cells, assessed by flow cytometry. **d**, Colony-forming units (c.f.u.) per ml of whole blood ($n = 10$ mice each). **e**, Dot plots of bone marrow neutrophils and monocytes. Gating was performed in the sequence indicated by the arrow for the highlighted gates from top to bottom. Numbers indicate the percentage of cells of the parent gate. The experiment was repeated twice with similar results. **f,g**, Number of monocytes (**f**) and neutrophils (**g**) per femur ($n = 10$ mice per group). Data in **a–d**, **f** and **g** were analysed using two-sided *t*-test. Data are shown as mean ± s.e.m.

we observed the highest fluorescence intensity in CD45$^-$CD31$^+$ Sca-1$^+$ endothelial cells, nanoparticle uptake into CD45$^+$ leukocytes was minimal (Fig. 2e). Uptake into other bone marrow cells (Supplementary Fig. 2), and into leukocytes and endothelial cells in other organs (Supplementary Fig. 3a,b) was lower than for BMECs. Such uptake, especially in organs that eliminate drugs or nanoparticles from the bloodstream, is to be expected. Macroscopic fluorescence imaging of key organs 2 h after intravenous injection of NicheEC-15 encapsulating fluorescently labelled siRNA revealed strong fluorescence in the femur marrow (Supplementary Fig. 3c–f). Compared to a previously described lipidoid nanoparticle with dominant uptake in the liver[21] and immune cells[18], NicheEC-15 bone marrow uptake was higher (Supplementary Fig. 3g). The avidity of NicheEC-15 nanoparticles for podoplanin$^-$ arteriolar and podoplanin$^+$ sinusoidal BMECs[30] was confirmed by ImageStream (Fig. 2f–i), which indicates uptake into major bone marrow endothelial cell subsets. Cell imaging detected no NicheEC-15-associated fluorescence in bone marrow leukocytes (Fig. 2j–l).

We next benchmarked NicheEC-15 to 7C1[19] in vivo. Compared to 7C1, NicheEC-15 uptake into BMECs increased significantly, while uptake into lung endothelial cells decreased (Fig. 2m). Although 7C1 uptake was similar in both organs, NicheEC-15 exhibited a threefold higher uptake into bone marrow endothelial cells (Fig. 2n), a result that supports NicheEC-15's higher avidity for the marrow over the lung. Furthermore, directly comparing *Tie2* in lung and bone marrow showed that NicheEC-15 enhances gene silencing in bone marrow while reducing such effects in lung, compared to 7C1 (Fig. 2o). Such a predilection may allow for high silencing efficiency in the marrow at lower doses.

Sdf1/Mcp1 target screening. Having identified NicheEC-15 as a delivery material, we proceeded to implement RNAi for modulating the haematopoietic bone marrow niche. We began by selecting two target proteins that influence haematopoietic stem cell and leukocyte behaviour: stromal-derived factor 1 (Sdf1, also known as Cxcl12) and monocyte chemotactic protein 1 (Mcp1, also known as Ccl2). These
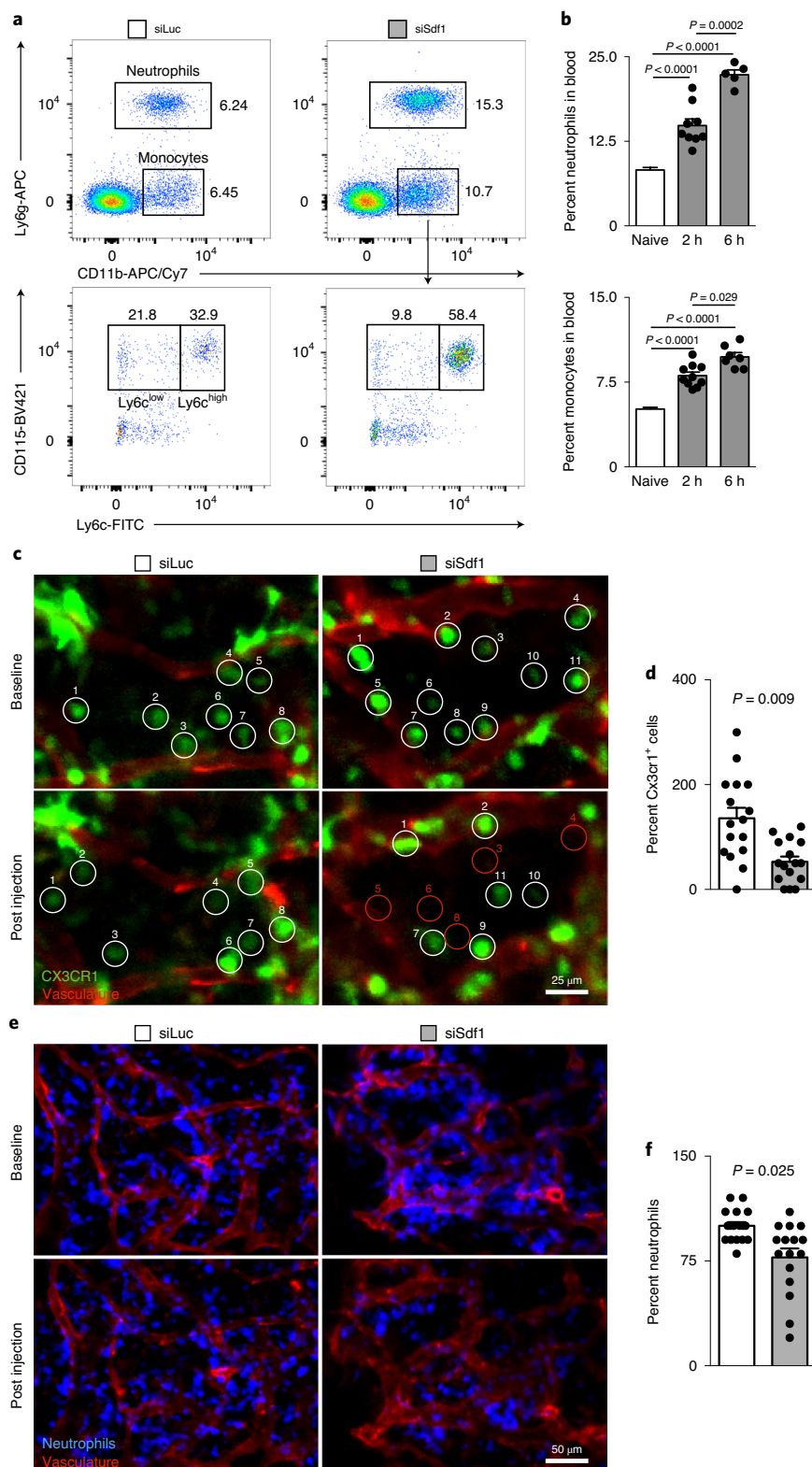
Fig. 4 | Release of bone marrow monocytes and neutrophils after siSdf1 treatment. a, Representative dot plots 2 h after injection. The numbers shown indicate the percentage of cells of the parent gate. The experiment was repeated twice with similar results. **b**, Percentage of neutrophils (top) and monocytes (bottom) in the blood, assessed by flow cytometry ($n = 10$ mice for naive and 2 h, $n = 5$ mice for 6-h neutrophils and $n = 7$ mice for 6-h monocytes; two-way ANOVA with multiple comparisons). **c**, Intravital microscopy imaging of Cx3cr1+ cells in the skull bone marrow. Baseline images were taken before injection and cells were tracked by imaging every 10–30 min for a total of 2.5 h. The locations of cells compared to baseline and at the last imaging after 2.5 h are indicated with white circles. Red circles mark the areas of cells that have left the niche. **d**, Percentage of Cx3cr1+ cells in the same area after 2.5 h compared to baseline, which was adjusted to 100% ($n = 4$ mice each, four fields of view per mouse; two-sided t-test). **e**, The same set-up as in **c**, but neutrophils are labelled with Ly6g antibody. **f**, As in **d**, the percentage of neutrophils after 2.5 h compared to baseline ($n = 4$ mice each, four fields of view per mouse; two-sided t-test). Data are shown as mean ± s.e.m.
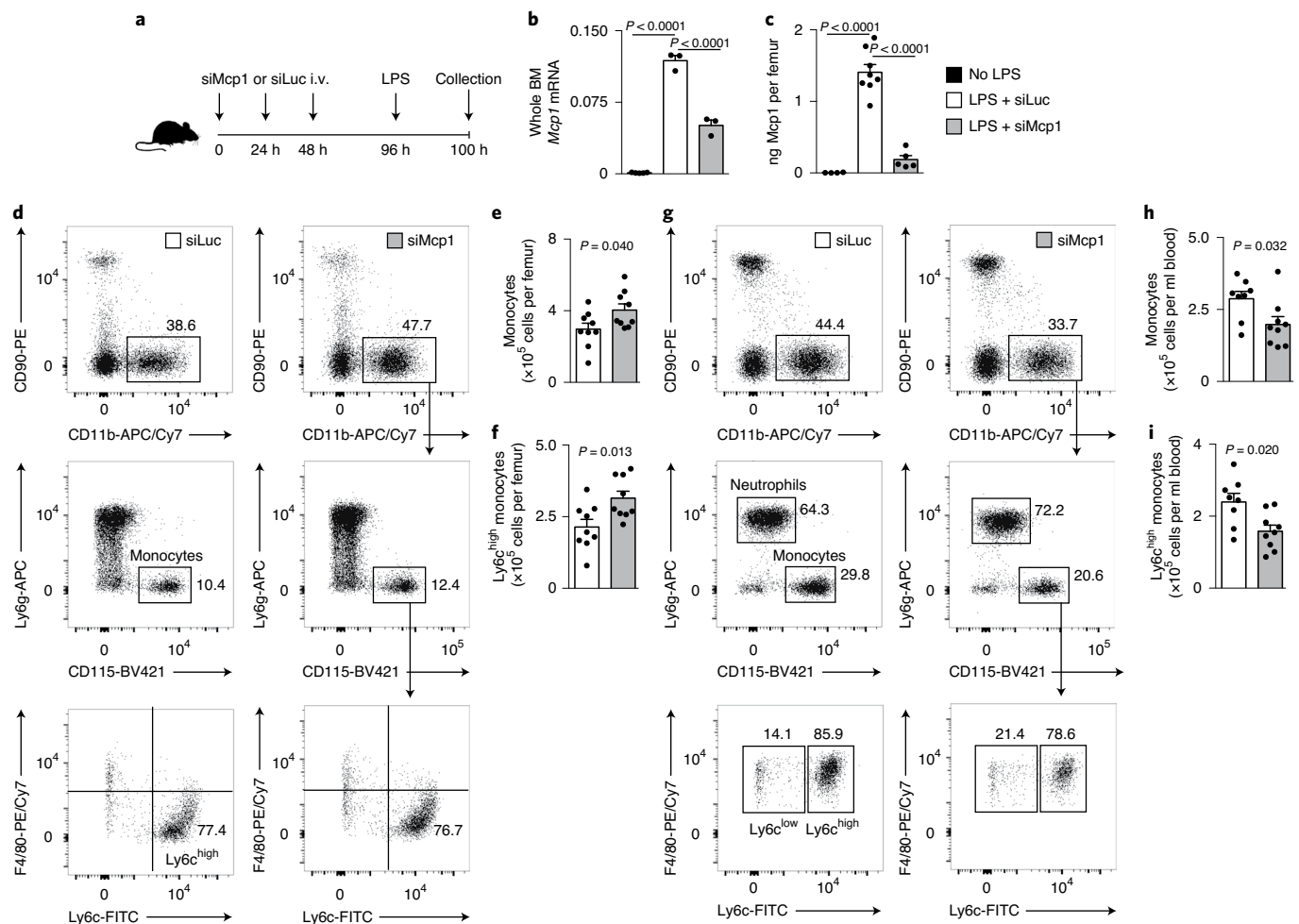
Fig. 5 | Effects of siMcp1 treatment during LPS-induced inflammation. a, Experimental set-up. **b**, *Mcp1* expression in whole bone marrow by qPCR normalized to GAPDH expression ($n = 3$ mice per group, except 'No LPS' $n = 5$; two-way ANOVA with multiple comparisons). **c**, Mcp1 levels by enzyme-linked immunosorbent assay (ELISA) in bone marrow plasma ($n = 4$, 7 and 5 mice per group, respectively; two-way ANOVA with multiple comparisons). **d**, FACS plots of bone marrow neutrophils and monocytes. Numbers shown indicate the percentage of cells of the parent gate. Gating was performed from top to bottom as indicated by the arrows. The experiment was repeated twice with similar results. **e**, Number of monocytes per femur. **f**, Number of Ly6c^{high} monocytes per femur. **g**, FACS plots of blood neutrophils and monocytes. Numbers indicate the percentage of cells of the parent gate. Gating was performed from top to bottom as indicated by the arrows. The experiment was repeated twice with similar results. **h**, Number of monocytes per ml of blood. **i**, Number of Ly6c^{high} monocytes per ml of blood. In **e**, **f**, **h** and **i**, $n = 9$ mice per group each; two-sided *t*-test. Data are shown as mean ± s.e.m.

well-studied proteins[1,2,31,32] were chosen because their known functional properties allowed us to use specific functional in vivo assays; additionally, because these proteins control cellular quiescence and migration, they are interesting drug targets. Viable siRNA sequences targeting *Sdf1* (Supplementary Fig. 4) and *Mcp1* (Supplementary Fig. 5) were identified by in vitro screening of in silico-predicted candidates. The top four siRNA sequences silencing *Sdf1* (Supplementary Fig. 4a,b) and *Mcp1* (Supplementary Fig. 5a,b) were then screened in vitro with a dose–response assay. The siRNAs with the lowest half maximal inhibitor concentration (IC_{50}) and 80% of maximal inhibitor concentration (IC_{80}) were selected for scale-up, nanoparticle formulation and modification to minimize immunostimulation and off-target gene silencing[33]. The lead siRNA candidates encapsulated in NicheEC-15 nanoparticles induced potent, dose-dependent gene silencing of *Sdf1* (Supplementary Fig. 4c) and *Mcp1* (Supplementary Fig. 5c) at low dosages in endothelial cells in vitro.

siSdf1 triggers bone marrow cell release. After tail-vein injection of NicheEC-15 nanoparticles loaded with siRNA cargo targeting

Sdf1 (siSdf1), we found a greater than twofold decrease in *Sdf1* expression (Fig. 3a) and significantly decreased Sdf1 protein in the femur (Supplementary Fig. 6a). To explore the cellular target responsible for this effect, using fluoresence-activated cell sorting (FACS), we isolated bone marrow endothelial cells from mice after treatment with NicheEC-15 nanoparticles containing siSdf1. Indeed, compared to controls, *Sdf1* expression was strongly reduced in these cells (Fig. 3b) but not in other niche cells (Supplementary Fig. 6b–d). To evaluate the specificity of RNAi effects, we also examined the expression of two other genes that influence haematopoietic stem cell behaviour in the haematopoietic niche, *Vcam1* and *Scf*. As expected, no change in gene expression was observed in BMECs, osteoblasts or mesenchymal stromal cells after treatment with siSdf1 (Supplementary Fig. 6e,f).

Because Sdf1 retains HSPCs[31] and leukocytes[32] in the bone marrow, we proceeded to investigate HSPC migration to monitor the functional consequences of RNAi. Indeed, we observed higher lineage⁻ sca1⁺ c-kit⁺ (LSK) cell numbers in blood of mice treated with siSdf1 (Fig. 3c), indicating release of these progenitor cells from
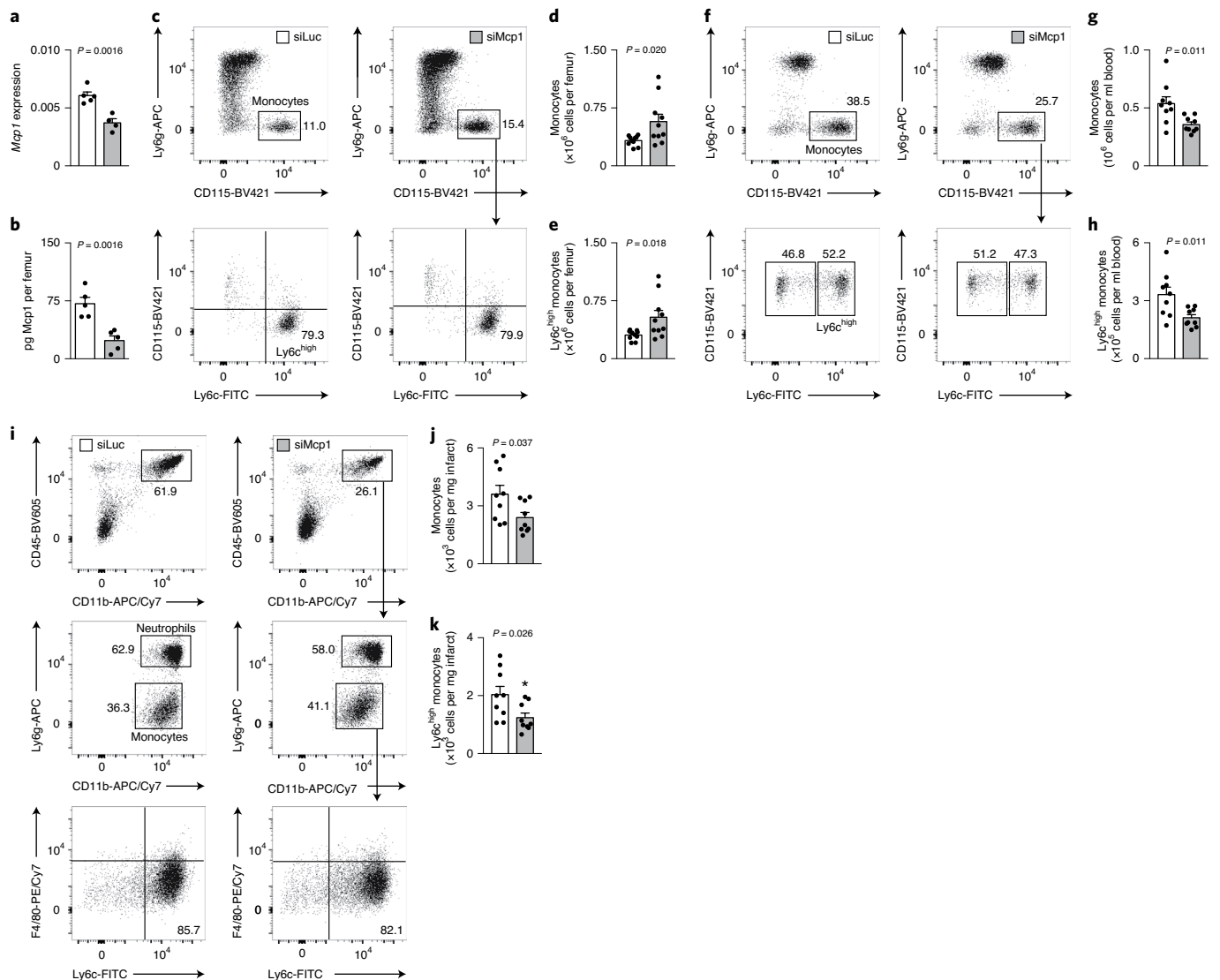
Fig. 6 | Effects of siMcp1 treatment on inflammatory cells 24 h after MI. a, *Mcp1* expression in whole bone marrow by qPCR normalized to GAPDH expression. **b**, Mcp1 levels, by ELISA, in bone marrow plasma. **c**, FACS plots of bone marrow monocytes. Numbers shown indicate the percentage of cells of the parent gate. Gating was performed from top to bottom as indicated by the arrows. In **a** and **b**, *n* = 5 mice per group each; two-sided *t*-test. **d**, Number of monocytes per femur. **e**, Number of Ly6c^high monocytes per femur. In **d** and **e**, *n* = 10 mice per group each; two-sided *t*-test. **f**, FACS plots of blood neutrophils and monocytes. Numbers shown indicate the percentage of cells of the parent gate. Gating was performed from top to bottom as indicated by the arrows. **g**, Number of monocytes per ml of blood. **h**, Number of Ly6c^high monocytes per ml of blood. **i**, FACS plots of the infarct. Numbers shown indicate the percentage of cells of the parent gate. Gating was performed from top to bottom as indicated by the arrows. **j**, Number of monocytes per mg infarct tissue. **k**, Number of Ly6c^high monocytes per mg infarct tissue. In **g**, **h**, **j** and **k**, *n* = 9 mice per group each; two-sided *t*-test. Data are shown as mean ± s.e.m.

the marrow. The increase in circulating HSPCs was confirmed by colony-forming unit (c.f.u.) assays in blood (Fig. 3d). Accordingly, siSdf1 injection decreased bone marrow LSK cells (Supplementary Fig. 6g,h). Similarly, downstream myeloid progenitors, including common myeloid progenitors (CMPs) and granulocyte macrophage progenitors (GMPs), declined in numbers in the femur after siSdf1 treatment (Supplementary Fig. 6i–k).

To investigate if RNAi leads to liberation of functional haematopoietic stem cells into the blood, we co-transplanted blood from siSdf1 and PBS-treated control mice into lethally irradiated recipients (Supplementary Fig. 7a). Eight weeks later, almost all leukocytes in the blood transplant recipients originated from siSdf1-treated mice (Supplementary Fig. 7b,c). The marrow of primary recipients was then used for a secondary transplantation into lethally

irradiated recipient mice. Nine of the ten recipient mice survived for six months, after which they exhibited high blood chimerism for major leukocyte subsets (Supplementary Fig. 7d,e). In a head-to-head comparison of RNAi-triggered bone marrow stem cell release versus results with the clinical drug AMD3100, which inhibits CXCR4 (the cognate receptor of Sdf1), and granulocyte colony-stimulating factor (G-CSF), we found that the siSdf1 treatment effects were positioned between those of AMD3100 and G-CSF (Supplementary Fig. 7f).

In addition to HSPC release, we also found that siSdf1 treatment leads to monocyte and neutrophil departure from the bone marrow (Fig. 3k–m). As a consequence, neutrophils and monocytes may become more numerous in the circulation. Because the level of circulating myeloid cells regulates their presence at sites of inflammation
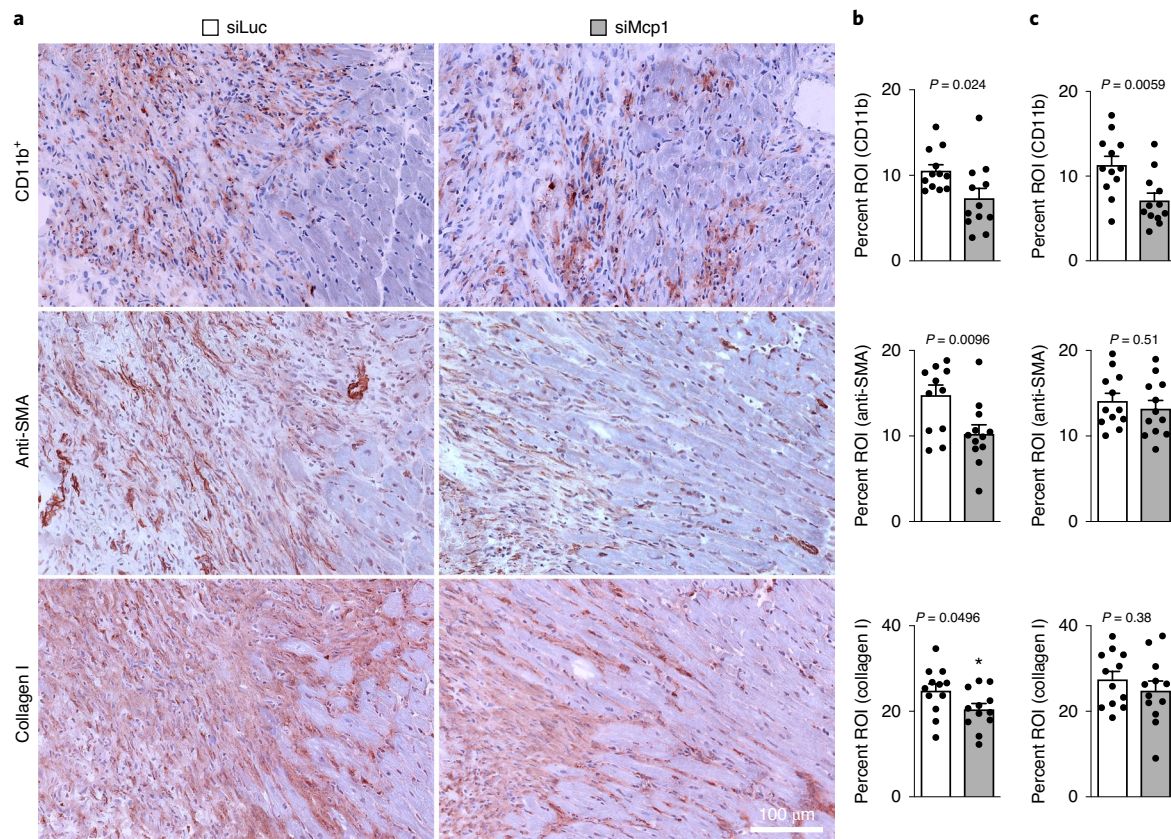
Fig. 7 | Cardiac effects of siMcp1 treatment seven days after MI. a, Immunohistochemical staining for myeloid cells (CD11b), anti-smooth muscle actin+ fibroblasts (anti-SMA) and collagen deposition (collagen I) in the border zone of the infarct. After 10 weeks of HFD starting at eight weeks of age, MI was induced by permanent ligation of the left anterior descending artery in ApoE$^{-/-}$ mice. Mice were either treated with siMcp1 or siLuc. **b**, Bar graphs showing the percentage of positive staining per region of interest (ROI) in the border zone of the infarct. **c**, Same analyses as in **b** but in the central infarct core. In **a**–**c**, $n = 4$ mice per group each and three fields of view per mouse; two-sided t-test. Data are shown as mean ± s.e.m.

and is associated with patient mortality, we studied the early dynamics of this leukocyte release. Two hours after siSdf1 injection, myeloid cells became significantly more abundant compared to baseline, and increased even further at 6 h (Fig. 4a,b). Such a boost in circulating leukocytes may also be caused by redistribution from other cell pools, such as in the lung or spleen. We thus used serial pre- and post-RNAi treatment intravital microscopy to survey the skull bone marrow. We visualized bone marrow macrophages and monocytes in Cx3cr1$^{GFP/+}$ mice before and up to 2.5 h after siSdf1 injection. By monitoring specific bone marrow niches, we were able to track individual cell behaviour over time (Fig. 4c). Treatment with siSdf1 triggered departure of Cx3cr1+ cells, although this was not observed after treatment with control siRNA (Fig. 4d). A similar dynamic was observed for neutrophils that we labelled in vivo with an Ly6g-APC antibody (Fig. 4e,f). In summary, these data demonstrate the ability to trigger stem cell and leukocyte release by silencing retention factors in the bone marrow vasculature.

siMcp1 inhibits bone marrow cell release. Although *Sdf1* silencing increased cell migration from the marrow, we next chose a gene target to explore the opposite functionality, that is, using RNAi to dampen leukocyte traffic. Such an intervention could be a therapeutic avenue to reduce systemic leukocyte supply in the setting of inflammation. Monocyte bone marrow departure is triggered by secretion of the chemokine Mcp1 into the sinusoidal space, for example after infection, injection of lipopolysaccharide (LPS, a building block of the bacterial wall that binds toll-like receptors)

or myocardial infarction (MI)[18,34]. Because monocytes express the cognate chemokine receptor Ccr2, they follow the Mcp1 chemokine gradient and extravasate from the niche into the bone marrow sinusoids. We tested the effect of *Mcp1* silencing in the setting of inflammation induced via the injection of LPS (Fig. 5a). As expected, LPS injection increased *Mcp1* expression in the marrow, and such expression was significantly reduced by siMcp1 treatment (Fig. 5b). Mcp1 protein levels were similarly elevated by LPS, which was abrogated by siMcp1 treatment (Fig. 5c). As a consequence, monocyte numbers in the bone marrow were higher in siMcp1-treated mice (Fig. 5d–f), whereas blood monocyte numbers decreased (Fig. 5g–i).

Mcp1/Ccr2 signalling also regulates monocyte migration in sterile inflammation, including during cardiovascular disease. In particular, acute MI triggers blood monocytosis, followed by cell recruitment into the ischaemic myocardium[35]. After MI, systemic oversupply of inflammatory monocytes may lead to heart failure and subsequent ischaemic events[10]. We therefore tested if silencing Mcp1 in mice with acute MI may reduce inflammatory Ly6c^{high} monocyte numbers in circulation and the heart. Treating mice with siMcp1 led to a lower bone marrow Mcp1 expression (Fig. 6a) and protein level (Fig. 6b). Consequently, monocyte bone marrow numbers rose (Fig. 6c,d), while circulating monocyte numbers remained lower (Fig. 6f–h), results that indicate attenuated cell release from the marrow. Ultimately, fewer monocytes, including the inflammatory Ly6C^{high} subset, were recruited to the infarcted heart in mice treated with siMcp1 (Fig. 6i–k).
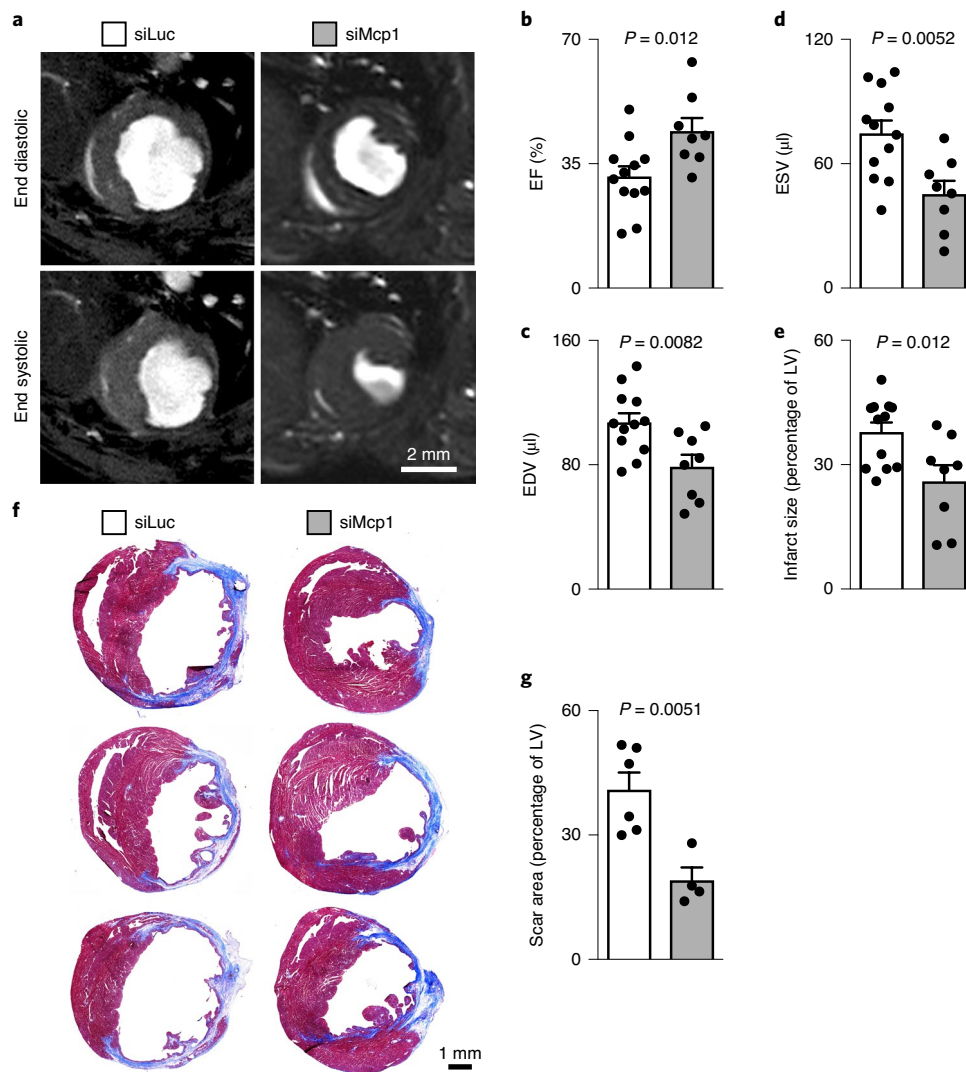
Fig. 8 | Therapeutic effects of siMcp1 on cardiac function and anatomy three weeks after MI. a, Short-axis magnetic resonance images three weeks after infarction. ApoE$^{-/-}$ mice were kept on HFD for 10 weeks (starting at 8 weeks of age), before induction of MI by permanent ligation of the left coronary artery. Mice were treated with siMcp1 or control siLUC. **b**, Left ventricular ejection fraction (EF). **c**, Left ventricular end-diastolic volume (EDV). **d**, End-systolic volume (ESV). **e**, Fraction of the infarcted left ventricular (LV) wall volume by MRI. In **a**–**e**, $n = 12$ versus 8 mice per group; two-sided t-test. **f**, Masson's trichrome staining, shown for $n = 3$ mice per group. **g**, The scar was calculated as the percent of left ventricular myocardium in three short-axis views obtained in individual mice ($n = 5$ mice each; two-sided t-test). Data are shown as mean ± s.e.m.

We evaluated the therapeutic consequences of siMcp1 on cardiovascular outcomes by studying the recovery from MI in ApoE$^{-/-}$ mice with hypercholesterolaemia and atherosclerosis. In these mice, gene deletion and high-fat diet (HFD) lead to blood monocytosis, which arises from increased haematopoiesis[36–38]. We previously described that the oversupply of monocytes in the post-MI phase disrupts the resolution of inflammation after cardiac ischaemia, leading to poor infarct healing and increased severity of heart failure[39,40]. Thus, these mice, like patients with atherosclerosis, hyperlipidaemia and monocytosis, hypothetically benefit from a dampened leukocyte supply to the infarct. ApoE$^{-/-}$ mice were given an atherogenic diet for 10 weeks before permanent coronary ligation. Mice were treated with three doses of control siRNA or siMcp1. We examined infarct healing histologically seven days after coronary ligation. In line with the flow cytometry data described above, RNAi treatment reduced staining for CD11b$^+$ myeloid cells in the border zone and the infarct core (Fig. 7a–d). We also observed a reduction of fibroblast numbers

and collagen content in the border zone, indicating that the treatment reduced inflammation and fibrosis.

Additional cohorts of ApoE$^{-/-}$ mice were examined three weeks after MI, when left ventricular remodelling gives rise to heart failure. Cardiac magnetic resonance imaging (MRI) reported that siMcp1 treatment preserved left ventricular anatomy and function when compared to siLuc-treated control ApoE$^{-/-}$ mice (Fig. 8a–e). Masson's trichrome staining revealed that the percentage of the left ventricle occupied by scar was lower in siMcp1-treated mice (Fig. 8f,g). Taken together, these data indicate that reduction of systemic monocyte supply by RNAi augmented recovery from MI.

Discussion

Bone marrow niche cells regulate haematopoietic and leukocyte activity in numerous ways, including cell transit into the circulation[1,2,41]. We have developed a nanoformulation capable of delivering siRNA to bone marrow niche cells. These nanoparticles are derivatives of prior materials with avidity for lung endothelial cells[19].

We enhanced nanoparticle siRNA delivery to the bone marrow by modulating nanoparticle PEG architecture, including (1) the molecular weight of the PEG surface coating, (2) the length of the lipid chain that anchors PEG within the nanoparticle membrane and (3) the PEG surface density. By screening polymer–lipid hybrid materials, combined with modulating PEG nanoparticle surface coatings, we obtained a nanoparticle, termed NicheEC-15, with superior avidity for and efficient silencing in bone marrow endothelial cells. We speculate that NicheEC-15, perhaps due to its denser PEG surface coat, escapes first-pass entrapment in the lung, which increases arterial circulation and uptake into bone marrow endothelial cells. The mechanism of uptake into bone marrow endothelial cells remains to be determined and may be subject to changes induced by pathologies or treatments such as irradiation or chemotherapy.

To test NicheEC-15, we silenced two prototypical haematopoietic niche factors. One of them, Sdf1, promotes stem cell quiescence and bone marrow retention of leukocytes via interaction with its cognate receptor Cxcr4. This pathway is currently targeted clinically using G-CSF and AMD3100, which trigger stem cell liberation into the blood[42]. Silencing HSPC retention factors using nanoparticle-enabled RNAi may improve the cell yield in stem cell transplantation, especially in patients that are poor stem cell mobilizers due to comorbidities such as diabetes[43]. Our second target, Mcp1, has the opposite effect, as this chemokine triggers bone marrow monocyte release. We found that silencing those proteins, using NicheEC-15 enabled RNAi, altered migration of HSPCs and leukocytes from bone marrow niches into the systemic blood pool. Our data provide a proof of principle that bone marrow HSPC and leukocyte behaviour may be addressed using RNAi therapeutics with avidity for the haematopoietic niche.

Owing to the modular character of RNAi, this approach can be adapted for silencing any other endothelial-cell-derived bone marrow niche factor, including growth hormones, cytokines and adhesion molecules that influence HSPC or leukocyte biology. Furthermore, silencing receptors may modulate the ability of endothelial cells to sense and relay information they receive from the circulation. The function of bone marrow niche cells in the steady state and disease is the subject of vibrant research, and large unbiased datasets (for example, obtained by RNA sequencing of bone marrow endothelial cells) are increasingly becoming available[44]. The technology we describe here is suitable for rapidly testing the function of highly expressed genes and newly arising drug candidates in vivo.

Endothelial cells separate bone marrow niches from the blood pool. Their barrier function, which ultimately regulates cell release, makes them a particularly attractive target for modulating cell migration. However, there are other niche cells that regulate haematopoiesis. Future materials may deliver siRNA to bone marrow macrophages, mesenchymal stromal cells or osteoblasts, thereby targeting other niche components. Such additions to the target cell portfolio may also facilitate RNAi for niche-driven malignancies.

Although we have focused on bone marrow cell release, which is of clinical interest in collecting stem cells before autologous haematopoietic bone marrow transplantation for leukaemia treatment, other haematopoietic cell functions could also be influenced. Stem cell quiescence and lineage bias are of particular interest as they decisively influence the size and function of any systemic blood cell pool. As demonstrated by silencing *Mcp1*, reducing the release of short-lived leukocytes from their site of production may dampen inflammation at any inflammatory site, including the ischaemic heart. Thus, reducing the oversupply of innate immune cells may curtail exuberant inflammatory activity in cardiovascular disease[10], the leading cause of death worldwide.

Methods

Synthesis of the polymer–lipid hybrid. Polymer–lipid hybrids were synthesized by reacting C15 alkyl epoxides (Tokyo Chemical Industry and Sigma) with PEI600 at 90 °C in 100% ethanol for 48–72 h at a 14:1 molar ratio. Because of the polydispersity index (PDI) of PEI600 ($M_n = 600$, PDI = 0.33), polymer–lipids were purified via high-performance liquid chromatography (HPLC) on a silica column with dichloromethane. MeOH and NH_4OH were added to the solvent over a 45-min period to decrease polarity, which enabled HPLC separation of the polymer–lipid into fractions related to the hydrophobic C15:hydrophilic PEI ratio. Mixtures were split into five fractions and individually assessed for their ability to induce gene silencing in mice.

siRNA nanoparticle synthesis. To formulate nanoparticles, polymer–lipid materials were combined with polyethylene (PEG)–lipid conjugates (Avanti Polar Lipids) and mixed with siRNA in a microfluidic device. Polymer–lipids and PEG–lipid conjugates were dissolved in 200-proof ethanol and loaded into a gas-tight Hamilton glass syringe, with siRNA held in 10 mM citrate buffer (pH 3.0; Teknova). Syringes were connected to the inlets of a microfluidic device containing static mixers, and the contents were perfused through the device to formulate nanoparticles. The nanoparticle formulations were sterile-filtered against PBS using a 20,000-molecular-weight-cutoff dialysis cassette (Thermo Scientific) to remove citrate and ethanol. Nanoparticle size and structure were determined by both DLS using a Zetasizer Nano ZS machine (Malvern Instruments) and cryo-TEM using a Tecnai 12 G2 transmission electron microscope (FEI). Nanoparticle samples were prepared in a vitrification system (25 °C, ~100% humidity), and images of samples were recorded on an UltraScan 1000 charge-coupled device camera (Gatan) in low-dose conditions. For zeta potential measurements, nanoparticles (25 μl) at a polymer–lipid concentration of 1 mg ml^{-1} were added to PBS (1 ml) and measured using a Malvern Zetasizer Nano ZS machine (mean, −0.15 mV; s.d., 9.28). The concentration of siRNA used for in vitro and in vivo treatment was quantified using both a Quant-iTTM Ribogreen assay (Invitrogen) and NanoDrop measurements (Thermo Scientific).

Cell culture. The endothelial cell line bEnd.3 (CRL-2299, ATCC) was cultured in Dulbecco's modified Eagle's medium, supplemented with 10% (vol/vol) fetal bovine serum and 1% (vol/vol) penicillin/streptomycin under humidified conditions at 37 °C and 5% CO_2 until cell confluence. To investigate knockdown efficiency, bEnd.3 cells were plated in 24-well plates (150,000 cells per well) and incubated for 24 h before treatment with nanoparticles formulated with siRNA targeting one of the following genes: luciferase (*LUC*), monocyte chemoattractant protein 1 (*Mcp1*) or stromal-derived factor-1 (*Sdf1*). A serial dilution of each siRNA nanoparticle formulation in PBS was prepared at concentrations of 1–60 nM siRNA. Samples were then incubated for 24 h before gene expression analysis. Cells were washed with PBS and collected using 0.25% trypsin. RNA was extracted from cells using an Arcturus PicoPure RNA isolation kit (Thermo Scientific). To study the in vitro uptake of NicheEC-15 by microscopy, bEnd.3 cells were plated in six-well plates (500,000 cells per well) and grown until confluence. NicheEC-15 containing Alexa Fluor 647 coupled luciferase siRNA was then added at a concentration of 200 nM RNA 2 h before imaging. At 15 min before imaging, 5 μM Syto 13 Green (Life Technologies) and 5 μg ml^{-1} wheat germ agglutinin Alexa Fluor 555 (WGA, Life Technologies) were added. During the last 5 min the cell cultures were washed repeatedly with PBS. The controls were treated identically, except that NicheEC-15 containing unlabelled luciferase siRNA was used. All steps except washing were done under humidified conditions at 37 °C and 5% CO_2.

Mice. All animal procedures conducted at Massachusetts General Hospital and Massachusetts Institute of Technology were approved by the Institutional Animal Care and Use Committees and were in accordance with local, state and federal regulations. C57BL/6J (Jackson Laboratory, stock no. 000664), B6.129P-Cx3cr1$^{tm1Litt/J}$ (Jackson Laboratory, stock no. 005582) and B6.SJL-Ptprc^{a}Pepc^b/BoyJ (Jackson Laboratory, stock no. 002014) mice were used at 11 to 13 weeks of age. To obtain hemizygous B6.129P-Cx3cr1$^{tm1Litt/J}$ mice, homozygous mice were crossed with C57BL/6J mice. Nanoparticles were administered by tail-vein injection. Myocardial infarction was induced by permanent coronary ligation in B6.129P2-Apoe^{tm1Unc}/J mice (Jackson Laboratory, stock no. 002052) after 10 weeks of HFD (Envigo Teklad Diets, stock no. TD.88137), starting at eight weeks of age and as previously described[29]. Briefly, mice were anaesthetized, given buprenorphin subcutaneously for analgesia, intubated and ventilated with 2% isoflurane supplemented with oxygen. After thoracotomy, the heart was exposed and the left coronary artery was identified and permanently ligated with a monofilament nylon 8–0 suture. For the LPS model, after nanoparticle treatment, 100 μl of normal saline containing 2 ng LPS (Sigma) was injected i.v. and the mice were collected 4 h after LPS injection.

Gene silencing. For gene silencing in whole femoral bone marrow, mice were euthanized by CO_2 asphyxiation, and femurs were collected and immediately snap-frozen in liquid nitrogen. Frozen tissues were pulverized to form a powder using a SPEX 2010 Geno/Grinder (SPEX SamplePrep). Tissue lysates were prepared in tissue and cell lysis buffer (Epicentre) supplemented with 0.5 mg ml^{-1} proteinase K (Epicentre). Tissue samples were mixed at 1,400 r.p.m. for 2 h at 65 °C and centrifuged at 16,000 r.c.f. to remove bone debris. mRNA levels in the supernatant were quantified using the QuantiGene 2.0 luminescent-based

branched DNA (bDNA) assay kit and QuantiGene 2.0 probes against Tie2 and GAPDH (Thermo Fisher Scientific), according to the manufacturer's protocol. Luminescent signals were measured using a Tecan Infinite 200 PRO plate reader (Tecan). Standard curves for femur tissues and each target gene were constructed using samples from untreated mice to ensure optimal dilutions for assay samples that avoid luminescent signal saturation. Targeted gene silencing in treated mice was quantified by calculating the ratio of target gene luminescence to *Gapdh* gene luminescence, with all values normalized to target gene:*Gapdh* gene ratios from control mice.

Flow cytometry and sorting. Single-cell suspensions were obtained from peripheral blood, bone marrow, aorta and lung. Briefly, blood was collected by eye bleeding using heparinized capillaries or, if larger volumes were needed, by cardiac puncture and addition of 10 mmol l^{-1} EDTA per 100 µl of blood. Red blood cell lysis was achieved by adding 1× red blood cell lysis buffer (Biolegend) for 2 min. After blood collection, mice were perfused through the left ventricle with 30 ml of ice-cold PBS after cutting the inferior vena cava. Bone marrow was collected by flushing femurs in PBS with 0.5% bovine serum albumin for leukocyte and HSPC staining or with HBSS containing 2 mg ml^{-1} Dispase (Sigma), DNaseI (Sigma) and 1 mg ml^{-1} collagenase IV and incubated with gentle agitation for 30 min at 37 °C to extract endothelial cells. To extract endothelial cells from solid tissues, organs were minced with fine scissors and incubated in the same digestion mix as bone marrow. Osteoblasts were collected by crushing the femur and digesting the bone fragments in PBS with 1 mg ml^{-1} collagenase I (Gibco) and DNaseI (Sigma) Tissues were then plunged through a 70-µm nylon mesh (BD Falcon), washed and centrifuged (8 min, 300*g*, 4 °C). The obtained single-cell suspensions were stained at 4 °C for 30 min and afterwards washed, centrifuged and resuspended. We used the following fluorochrome- and biotin-conjugated antibodies specific to mouse: B220 (clone RA3–6B2), CD3e (clone 145–2C11), CD4 (clone GK1.5), CD8a (clone 53–6.7), CD11b (clone M1/70), CD11c (clone HL3), CD16/32 (clone 93 and 2.4G2), CD19 (clone 1D3), CD31 (clone MEC13.3), CD34 (clone RAM34), CD41 (clone MWReg30), CD45 (clone 30-F11), CD45.1 (clone A20), CD45.2 (clone 104), CD51 (BioLegend, cat no. 104106, clone RMV-7), CD48 (HM48–1), CD90.2 (clone 53–2.1), CD115 (clone AFS98), CD150 (clone TC15–12F12.2), c-kit (clone 2B8), F4/80 (clone BM8), GR1 (clone RB6–8C5), IL7Rα (clone A7R34), Ly6C (clone AL-21), Ly-6G (clone 1A8), NK1.1 (clone PK136), PDGFRa (CD140a, clone APA5), podoplanin (clone 8.1.1), Sca-1 (clone D7) and Ter119 (clone TER119). Antibodies were purchased from Biolegend, BD Biosciences or eBioscience. Monocytes were identified as CD90$^-$ CD19$^-$ NK1.1$^-$ Ly-6G$^-$ D45.2$^+$ CD11b^{high} CD115$^+$ F4/80^{low} and separated into Ly6C^{low} and a Ly6C^{high} populations. Neutrophils were identified as CD90$^-$ CD19$^-$ NK1.1$^-$ D45.2$^+$ CD11b^{high} Ly-6G$^+$, T cells as CD11b$^-$ CD19$^-$ NK1.1$^-$ CD45$^+$ CD90/CD4$^+$ and B cells as CD11b$^-$ CD90/CD4$^-$ NK1.1$^-$ CD45$^+$ CD19$^+$. Blood and bone marrow LSK cells were identified as (B220 CD3e CD4 CD8a CD11b CD11c CD19 CD90.2 GR1 IL7Ra NK1.1 Ter119)$^-$ c-kit$^+$ Sca-1$^+$, LKs as (B220 CD3e CD4 CD8a CD11b CD11c CD19 CD90.2 GR1 NK1.1 Ter119)$^-$ c-kit$^+$ Sca-1$^-$, and subdivided into CMP, megakaryocyte–erythroid progenitor cells (MEP) and GMP by their CD16/32 and CD34 expression. Endothelial cells were gated as CD45.2$^-$ Ter119$^-$ CD31$^+$ Sca-1$^+$. Sinusoidal endothelial cells were distinguished by podoplanin expression (podoplanin$^+$) from arteriolar endothelial cells (podoplanin$^-$). Osteoblasts were gated as CD45$^-$ Ter119$^-$ CD31$^-$ PDGFRa$^+$ CD51$^+$ Sca-1$^-$ and mesenchymal stromal cells as CD45$^-$ Ter119$^-$ CD31$^-$ Sca-1$^-$ Lepr^{YFP+}. To define positivity for AF647-siRNA uptake, we used cells from uninjected mice as a negative control. Data were acquired on an LSRII system (BD Biosciences) and analysed with FlowJo software (Tree Star). For cell sorting, the populations were defined as described and sorted using a FACSAria II cell sorter. The cells were directly sorted into lysis buffer, and the samples were vortexed, quick frozen on dry ice and stored at −80 °C until RNA extraction.

mRNA extraction and qPCR. mRNA extraction and qPCR were performed as published previously and reproduced from ref. [29]. mRNA was extracted from cells using an Arcturus PicoPure RNA isolation kit (Thermo Scientific) for cultured and sorted endothelial cells, and the RNeasy Mini Kit (Qiagen) was used for whole bone marrow samples, both according to the manufacturers' protocols. mRNA concentration was measured using a NanoDrop 2000c Spectrophotometer (Thermo Scientific) or using a 2100 Bioanalyzer (Agilent) for low mRNA concentration. Yield was calculated and the same amount of mRNA was transcribed to complementary DNA (cDNA) using a high-capacity RNA to cDNA kit and Taqman primers (all Applied Biosystems). Results were expressed as Ct values after normalization to *Gapdh* as the housekeeping gene.

Imaging flow cytometry data acquisition and analysis. We used an ImageStream^X Mk II imaging flow cytometer (IFC; Amnis Corporation) equipped with two cameras and 12 channels to acquire images from bright-field (BF/Ch-01 or Ch-09) and dark-field (SSC/Ch-12) channels for each cell. INSPIRE version 200.1.620.0 instrument software was used for instrument set-up, calibration and data acquisition. Laser power settings were as follows: 405 nm at 80 mW; 488 nm at 150 mW; 642 nm at 150 mW; 785 nm (SSC) at 1.00 mW; 100–150-µl samples were loaded and multiple 100,000 event files were acquired at ×60 magnification for each sample. The acquired RIF files were later merged and analysed using the

software IDEAS version 6.2.64.0. A total of 1,000 event single-colour compensation controls were collected (w/o BF or SSC) and later merged to create a compensation matrix for analysis. Once the RIF files were merged and compensated, a gating strategy similar to the flow cytometry gating of BMECs was used for consistency: a bivariate plot of CD45/Ter119 versus SSC was first generated. Events negative for CD45/Ter119 were then used as a parent population for generation of a bivariate plot of Sca-1 versus CD31. Double-positive events were gated, visually verified as endothelial cells and confirmed to contain nanoparticle AF647 by imagery.

Drug-induced stem cell release assay. To compare the release of stem cells into the peripheral blood after siSdf1, AMD3100 and G-CSF treatment, four groups of mice were formed. The control group received no injections, the siSdf1 group was treated once daily with 2 mg kg^{-1} siSDF1 for three consecutive days then collected 24 h after the last injection. In the AMD3100 group, mice received an injection of 5 mg kg^{-1} 3 h before collection, and in the G-CSF group, mice were treated for five consecutive days with 250 µg kg^{-1} daily, and collected 12 h after the last injection. All mice were collected at the same time and 100 µl of peripheral blood was drawn for c.f.u. assay.

Colony-forming unit assay. C.f.u. assays were performed using a semisolid cell culture medium (Methocult M3434, Stem Cell Technology) following the manufacturer's protocol; 100 µl of whole blood was processed following the protocol, plated on 35-mm plates in duplicates and incubated for 10 days. Colonies were counted using a low-magnification inverted microscope.

Competitive peripheral blood transplantation and secondary bone marrow transplantation. For the primary, competitive peripheral blood transplantation[45–47] CD45.1$^+$ mice received lethal irradiation (9.5 Gy) 24 h before transplantation. CD45.2$^+$ donor mice received consecutive injections of 2 mg kg^{-1} siSdf1 every 24 h for three days while another batch of CD45.1$^+$ control mice were injected with PBS. At 24 h after the last injection, the blood of the siSdf1-treated CD45.2$^+$ and the CD45.1$^+$ control mice was collected by cardiac puncture, red blood cells were lysed by adding red blood cell lysis (RBCL) buffer for 2 min, the cells were washed by adding 20 ml of cold PBS, spun down (5 min, 300 r.p.m.) and resuspended for counting. Nucleated blood cells (1×10^8) from CD45.2$^+$ and CD45.1$^+$ mice were pooled and injected through the tail vein into lethal-irradiated recipient mice. Eight weeks later, blood chimerism was analysed by drawing 50 µl of blood for flow cytometry.

For the secondary transplant, another batch of CD45.1$^+$ recipient mice were lethally irradiated (9.5 Gy) 24 h before transplantation. On the day of the transplantation, femoral bones of mice from the first, competitive blood transplantation experiment were collected. The bone marrow was flushed out with cold PBS, plunged through a 40-µm cell strainer and centrifuged (5 min, 300 rpm), then red blood cells were lysed for 2 min with RBCL buffer, centrifuged again and resuspended in PBS with 5% albumin for counting. Each lethally irradiated, secondary recipient CD45.1$^+$ recipient mouse was transplanted with 5×10^6 bone marrow cells by tail-vein injection. Six months after secondary transplantation blood chimerism was analysed by drawing 50 µl of peripheral blood.

Fluorescence reflectance imaging. For biodistribution imaging, mice were euthanized 2 h after injection of 2 mg kg^{-1} encapsulated siRNA labelled with a near-infrared fluorochrome. Main organs were then collected and imaged on a planar fluorescent reflectance imaging system (OV-110, Olympus) with an excitation wavelength of 630 nm and exposure times of 60–75 m.

Intravital microscopy. To visualize the in vivo uptake of NicheEC-15 in bone marrow endothelial cells, we imaged the skull bone marrow as described previously[29]. OsteoSense was injected i.v. 24 h before imaging, NicheEC-15 AF647-siRNA 2 h before and PE-labelled CD31 and Sca-1 antibodies 1 h before.

Magnetic resonance imaging. ApoE$^{-/-}$ mice were kept on HFD for 10 weeks starting at age 8 weeks, before induction of MI by permanent ligation of the left coronary artery. Mice were treated with either siMCP1 or control siLUC (2 mg kg^{-1}) four days before MI, the day of MI induction and two days after induction. Mice were imaged 21 days after infarct induction on a Bruker 4.7 Tesla Pharmascan magnetic resonance imaging system with a stack of contiguous short-axis slices covering the entire left ventricle. We used a cine intragate fast low angle shot (FLASH) sequence with the following parameters: echo time, 2.945 ms; repetition time, 12.0 ms; flip angle, 45°; oversampling, 300; matrix size, 200 × 200; pixel size, 0.150 × 0.150 mm; slice thickness, 1 mm; number of movie frames per cycle, 16. The left ventriclular myocardium and cavity were segmented manually at diastole and systole using Horos software to calculate the ejection fraction and volume of the left ventricle. In addition, the percentage of the left ventricle that was infarcted was also determined manually by segmenting the infarct area.

Histology. To investigate bone marrow vessel density, mice were euthanized and femurs were removed seven days after injection of siSdf1 (2 mg kg^{-1}), siTie2 (2 mg kg^{-1}) or PBS as control. The femurs were fixed in fresh 4% paraformaldehyde at 4 °C overnight and then decalcified in 0.5 M EDTA solution (Sigma-Aldrich)

for 14 days by exchanging the solution every two days. After decalcification, the femurs were paraffin-embedded and serial sections were prepared for immunohistochemistry. The sections were deparaffinized, dehydrated and blocked with 3% H_2O_2 in methanol for 30 min at room temperature before staining. An endomucin antibody (Abcam ab106100) was incubated at 4 °C overnight and a biotinylated anti-rat IgG antibody (Dako) at room temperature for 30 min. A TSA Biotin System Kit (PerkinElmer) and DAB (Vector Laboratories) were used to visualize the staining, and the sections were counterstained with Fast Green (Sigma-Aldrich).

For histological evaluations of hearts after MI in ApoE$^{-/-}$ mice fed on HFD with siMcp1 (2 mg kg^{-1}) or siLuc treatment before and after surgery, mice were euthanized and hearts were perfused thoroughly with PBS and harvested. The hearts were embedded in optimal cutting temperature compound (Sakura Finetek) and subsequently snap-frozen in a 2-methylbutane bath cooled with dry ice. For the scar area assessment, Masson's trichrome staining was performed according to the manufacturer's instructions (Sigma-Aldrich). For each individual mouse, three evenly spaced short-axis sections of the left ventricle were collected that sampled the infarct from basal to apical regions. The infarct size was calculated as (scar area slide 1 + scar area slide 2 + scar area slide 3) / (remote area slide 1 + remote area slide 2 + remote area slide 3) × 100%. For immunohistochemistry, 6-µm frozen sections were stained using antibodies: CD11b (BD Biosciences, clone M1/70), alpha-smooth muscle actin (αSMA, Abcam ab5694) and collagen I (Abcam ab21286). The appropriate biotinylated secondary antibodies followed by the VECTASTAIN ABC kit (Vector Laboratories) were applied and AEC (3-amino-9-ethylcarbazole) substrate (Dako) was used for colour development. The sections were counterstained with Harris haematoxylin (Sigma-Aldrich). All the slides were scanned using a digital scanner (NanoZoomer 2.0RS, Hamamatsu) and quantification was performed using ImageJ. Three high-power fields per section per animal were analysed.

Enzyme-linked immunosorbent assay. ELISAs for Sdf1 and Mcp1 (both R&D) in the bone marrow were performed by spinning (11,000g, 2 min, 4 °C) the bone marrow out of one femur and taking the supernatant for ELISAs, which were performed according to the manufacturer's instructions.

Statistics. The statistics were performed as published previously[29]. Data are expressed as mean ± s.e.m. Statistical analyses were performed using Prism (Version 7, GraphPad Software). Two-sided Student's t-test was used when two groups were compared and the pre-test for normality (D'Agostino–Pearson normality test; significance level 0.05) was not rejected. For nonparametric data, the Mann–Whitney test was used. If more then two groups were compared, two-sided ANOVA tests followed by Bonferroni post-tests were applied. P values smaller than 0.05 indicate statistical significance.

Reporting Summary. Further information on research design is available in the Nature Research Reporting Summary linked to this Article.

Data availability
The main data supporting the results in this study are available within this paper and its Supplementary Information. The raw and analysed datasets generated during the study are too large to be publicly shared, but they are available for research purposes from the corresponding authors on reasonable request.

References
1. Morrison, S. J. & Scadden, D. T. The bone marrow niche for haematopoietic stem cells. *Nature* **505**, 327–334 (2014).
2. Mendelson, A. & Frenette, P. S. Hematopoietic stem cell niche maintenance during homeostasis and regeneration. *Nat. Med.* **20**, 833–846 (2014).
3. Crane, G. M., Jeffery, E. & Morrison, S. J. Adult haematopoietic stem cell niches. *Nat. Rev. Immunol.* **17**, 573–590 (2017).
4. Kaplan, R. N., Psaila, B. & Lyden, D. Niche-to-niche migration of bone-marrow-derived cells. *Trends Mol. Med.* **13**, 72–81 (2007).
5. Sipkins, D. A. et al. In vivo imaging of specialized bone marrow endothelial microdomains for tumour engraftment. *Nature* **435**, 969–973 (2005).
6. Butler, J. M. et al. Endothelial cells are essential for the self-renewal and repopulation of Notch-dependent hematopoietic stem cells. *Cell Stem Cell* **6**, 251–264 (2010).
7. Katayama, Y. et al. Signals from the sympathetic nervous system regulate hematopoietic stem. *Cell* **124**, 407–421 (2006).
8. Gratwohl, A. et al. Hematopoietic stem cell transplantation: a global perspective. *JAMA* **303**, 1617–1624 (2010).
9. Giralt, S. et al. Optimizing autologous stem cell mobilization strategies to improve patient outcomes: consensus guidelines and recommendations. *Biol. Blood Marrow Transpl.* **20**, 295–308 (2014).
10. Swirski, F. K. & Nahrendorf, M. Leukocyte behavior in atherosclerosis, myocardial infarction and heart failure. *Science* **339**, 161–166 (2013).
11. Calado, R. T. & Young, N. S. Telomere maintenance and human bone marrow failure. *Blood* **111**, 4446–4455 (2008).
12. Seo, A. et al. Bone marrow failure unresponsive to bone marrow transplant is caused by mutations in THPO. *Blood* **130**, 875–880 (2017).
13. Whitehead, K. A., Langer, R. & Anderson, D. G. Knocking down barriers: advances in siRNA delivery. *Nat. Rev. Drug Discov.* **8**, 129–138 (2009).
14. Titze-de-Almeida, R., David, C. & Titze-de-Almeida, S. S. The race of 10 synthetic RNAi-based drugs to the pharmaceutical market. *Pharm. Res.* **34**, 1339–1363 (2017).
15. Anselmo, A. C. & Mitragotri, S. Nanoparticles in the clinic. *Bioeng. Transl. Med.* **1**, 10–29 (2016).
16. Yin, H. et al. Non-viral vectors for gene-based therapy. *Nat. Rev. Genet.* **15**, 541–555 (2014).
17. Kanasty, R., Dorkin, J. R., Vegas, A. & Anderson, D. Delivery materials for siRNA therapeutics. *Nat. Mater.* **12**, 967–977 (2013).
18. Leuschner, F. et al. Therapeutic siRNA silencing in inflammatory monocytes in mice. *Nat. Biotechnol.* **29**, 1005–1010 (2011).
19. Dahlman, J. E. et al. In vivo endothelial siRNA delivery using polymeric nanoparticles with low molecular weight. *Nat. Nanotechnol.* **9**, 648–655 (2014).
20. Dong, Y. et al. Lipopeptide nanoparticles for potent and selective siRNA delivery in rodents and nonhuman primates. *Proc. Natl Acad. Sci. USA* **111**, 3955–3960 (2014).
21. Love, K. T. et al. Lipid-like materials for low-dose, in vivo gene silencing. *Proc. Natl Acad. Sci. USA* **107**, 1864–1869 (2010).
22. Khan, O. F. et al. Ionizable amphiphilic dendrimer-based nanomaterials with alkyl-chain-substituted amines for tunable siRNA delivery to the liver endothelium in vivo. *Angew. Chem. Int. Ed.* **53**, 14397–14401 (2014).
23. Khan, O. F. et al. Dendrimer-inspired nanomaterials for the in vivo delivery of siRNA to lung vasculature. *Nano Lett.* **15**, 3008–3016 (2015).
24. Whitehead, K. A. et al. Degradable lipid nanoparticles with predictable in vivo siRNA delivery activity. *Nat. Commun.* **5**, 4277 (2014).
25. Khan, O. F. et al. Endothelial siRNA delivery in nonhuman primates using ionizable low-molecular weight polymeric nanoparticles. *Sci. Adv.* **4**, eaar8409 (2018).
26. Chen, D. et al. Rapid discovery of potent siRNA-containing lipid nanoparticles enabled by controlled microfluidic formulation. *J. Am. Chem. Soc.* **134**, 6948–6951 (2012).
27. Gref, R. et al. Stealth corona-core nanoparticles surface modified by polyethylene glycol (PEG): influences of the corona (PEG chain length and surface density) and of the core composition on phagocytic uptake and plasma protein adsorption. *Colloids Surf. B Biointerfaces* **18**, 301–313 (2000).
28. Owens, D. E. III & Peppas, N. A. Opsonization, biodistribution and pharmacokinetics of polymeric nanoparticles. *Int. J. Pharm.* **307**, 93–102 (2006).
29. Heidt, T. et al. Chronic variable stress activates hematopoietic stem cells. *Nat. Med.* **20**, 754–758 (2014).
30. Xu, C. et al. Stem cell factor is selectively secreted by arterial endothelial cells in bone marrow. *Nat. Commun.* **9**, 2449 (2018).
31. Cheng, M. & Qin, G. Progenitor cell mobilization and recruitment: SDF-1, CXCR4, α4-integrin and c-kit. *Prog. Mol. Biol. Transl. Sci.* **111**, 243–264 (2012).
32. Furze, R. C. & Rankin, S. M. The role of the bone marrow in neutrophil clearance under homeostatic conditions in the mouse. *FASEB J.* **22**, 3111–3119 (2008).
33. Whitehead, K. A., Dahlman, J. E., Langer, R. S. & Anderson, D. G. Silencing or stimulation? siRNA delivery and the immune system. *Annu. Rev. Chem. Biomol. Eng.* **2**, 77–96 (2011).
34. Serbina, N. V. & Pamer, E. G. Monocyte emigration from bone marrow during bacterial infection requires signals mediated by chemokine receptor CCR2. *Nat. Immunol.* **7**, 311–317 (2006).
35. Nahrendorf, M., Pittet, M. J. & Swirski, F. K. Monocytes: protagonists of infarct inflammation and repair after myocardial infarction. *Circulation* **121**, 2437–2445 (2010).
36. Swirski, F. K. et al. Ly-6C^{hi} monocytes dominate hypercholesterolemia-associated monocytosis and give rise to macrophages in atheromata. *J. Clin. Invest.* **117**, 195–205 (2007).
37. Tacke, F. et al. Monocyte subsets differentially employ CCR2, CCR5 and CX3CR1 to accumulate within atherosclerotic plaques. *J. Clin. Invest.* **117**, 185–194 (2007).
38. Yvan-Charvet, L. et al. ATP-binding cassette transporters and HDL suppress hematopoietic stem cell proliferation. *Science* **328**, 1689–1693 (2010).
39. Nahrendorf, M. et al. The healing myocardium sequentially mobilizes two monocyte subsets with divergent and complementary functions. *J. Exp. Med.* **204**, 3037–3047 (2007).
40. Panizzi, P. et al. Impaired infarct healing in atherosclerotic mice with Ly-6C^{hi} monocytosis. *J. Am. Coll. Cardiol.* **55**, 1629–1638 (2010).

41. Itkin, T. et al. Distinct bone marrow blood vessels differentially regulate haematopoiesis. *Nature* **532**, 323–328 (2016).
42. Broxmeyer, H. E. et al. Rapid mobilization of murine and human hematopoietic stem and progenitor cells with AMD3100, a CXCR4 antagonist. *J. Exp. Med.* **201**, 1307–1318 (2005).
43. Ferraro, F. et al. Diabetes impairs hematopoietic stem cell mobilization by altering niche function. *Sci. Transl. Med.* **3**, 104ra101 (2011).
44. Langen, U. H. et al. Cell-matrix signals specify bone endothelial cells during developmental osteogenesis. *Nat. Cell Biol.* **19**, 189–201 (2017).
45. Peranteau, W. H., Hayashi, S., Hsieh, M., Shaaban, A. F. & Flake, A. W. High-level allogeneic chimerism achieved by prenatal tolerance induction and postnatal nonmyeloablative bone marrow transplantation. *Blood* **100**, 2225–2234 (2002).
46. Kwarteng, E. O. & Heinonen, K. M. Competitive transplants to evaluate hematopoietic stem cell fitness. *J. Vis. Exp.* **114**, e54345 (2016).
47. Maryanovich, M. et al. The ATM–BID pathway regulates quiescence and survival of haematopoietic stem cells. *Nat. Cell Biol.* **14**, 535–541 (2012).

Author contributions

M.K.-G., M.J.M., M.J.S., D.G.A. and M.N. designed the experiments. M.J.S., O.F.K., G.C., P.P.G.G., S.C., Y.S., M.T., J.W., K.W., D.R., P.S.K., R.N., V.F., M.H., A.C., F.F.H., Y.I., S.P.S. and G.R.W. performed experiments and collected data. M.K.-G., M.J.M., F.K.S., R.L., D.G.A. and M.N. discussed the results and strategy. M.K.-G., M.J.M., D.G.A. and M.N. wrote the manuscript, which was edited by all co-authors. D.G.A. and M.N. supervised, directed and managed the study.

Competing interests

R.L. has served as an advisor to Alnylam Pharmaceuticals. For a list of entities with which R.L. is involved, compensated or uncompensated, see www.dropbox.com/s/yc3xqb5s8s94v7x/Rev%20Langer%20COI.pdf?dl=0. M.N. has received consulting fees unrelated to this work from Verseau, Gimv and IMF Therapeutics. The remaining authors declare no competing interests.

Additional information

Supplementary information is available for this paper at https://doi.org/10.1038/s41551-020-00623-7.

Correspondence and requests for materials should be addressed to D.G.A. or M.N.

Reprints and permissions information is available at www.nature.com/reprints.

Publisher's note Springer Nature remains neutral with regard to jurisdictional claims in published maps and institutional affiliations.

nature research

Corresponding author(s):   Matthias Nahrendorf and Daniel Anderson

Reporting Summary

Nature Research wishes to improve the reproducibility of the work that we publish. This form provides structure for consistency and transparency in reporting. For further information on Nature Research policies, see Authors & Referees and the Editorial Policy Checklist.

Statistical parameters

When statistical analyses are reported, confirm that the following items are present in the relevant location (e.g. figure legend, table legend, main text, or Methods section).

n/a	Confirmed	
☐	☒	The exact sample size (*n*) for each experimental group/condition, given as a discrete number and unit of measurement
☐	☒	An indication of whether measurements were taken from distinct samples or whether the same sample was measured repeatedly
☐	☒	The statistical test(s) used AND whether they are one- or two-sided *Only common tests should be described solely by name; describe more complex techniques in the Methods section.*
☐	☒	A description of all covariates tested
☐	☒	A description of any assumptions or corrections, such as tests of normality and adjustment for multiple comparisons
☐	☒	A full description of the statistics including central tendency (e.g. means) or other basic estimates (e.g. regression coefficient) AND variation (e.g. standard deviation) or associated estimates of uncertainty (e.g. confidence intervals)
☐	☒	For null hypothesis testing, the test statistic (e.g. F, t, r) with confidence intervals, effect sizes, degrees of freedom and P value noted *Give P values as exact values whenever suitable.*
☒	☐	For Bayesian analysis, information on the choice of priors and Markov chain Monte Carlo settings
☒	☐	For hierarchical and complex designs, identification of the appropriate level for tests and full reporting of outcomes
☐	☒	Estimates of effect sizes (e.g. Cohen's *d*, Pearson's *r*), indicating how they were calculated
☐	☒	Clearly defined error bars *State explicitly what error bars represent (e.g. SD, SE, CI)*

Our web collection on statistics for biologists may be useful.

Software and code

Policy information about availability of computer code

Data collection	LSR II flow cytometer with BD FACSDiva software.
Data analysis	FlowJo V9, PRISM V6, OsiriX DICOM Viewer V10, ImageJ V1.52, Horos V4.0

For manuscripts utilizing custom algorithms or software that are central to the research but not yet described in published literature, software must be made available to editors/reviewers upon request. We strongly encourage code deposition in a community repository (e.g. GitHub). See the Nature Research guidelines for submitting code & software for further information.

Data

Policy information about availability of data

All manuscripts must include a data availability statement. This statement should provide the following information, where applicable:

- Accession codes, unique identifiers, or web links for publicly available datasets
- A list of figures that have associated raw data
- A description of any restrictions on data availability

The main data supporting the results in this study are available within the paper and its Supplementary Information. The raw and analysed datasets generated during the study are too large to be publicly shared, yet they are available for research purposes from the corresponding authors on reasonable request.

Field-specific reporting

Please select the best fit for your research. If you are not sure, read the appropriate sections before making your selection.

☒ Life sciences   ☐ Behavioural & social sciences   ☐ Ecological, evolutionary & environmental sciences

For a reference copy of the document with all sections, see nature.com/authors/policies/ReportingSummary-flat.pdf

Life sciences study design

All studies must disclose on these points even when the disclosure is negative.

Sample size	Sample sizes were calculated on the basis of the predicted between-group difference and power needed to reach a p level of 0.05 (cutoff for statistical significance in this study).
Data exclusions	No data points were excluded.
Replication	Experiments were in general performed three times (two replications) to confirm the results. Experiments are only shown if replications were successful and all experimental results could be confirmed.
Randomization	Mice / cages were randomly allocated to the experimental groups.
Blinding	Given the need to properly formulate the nanoparticles, the researchers were not blinded to the components that were used to synthesize each formulation. Tie2 knockdown studies were conducted by an independent operator, who was unaware of the treatment conditions. ImageStream experiments were performed and analysed by a core facility unaware of the study rationale. MRI and biodistribution imaging were performed and analysed in a blinded fashion. Flow-cytometry experiments were performed and managed by only one researcher, which precluded blinding; but analysis, specifically FACS gating, was defined by negative controls and all FACS data were independently reviewed by M.N.

Reporting for specific materials, systems and methods

Materials & experimental systems

n/a	Involved in the study
☐	☒ Unique biological materials
☐	☒ Antibodies
☐	☒ Eukaryotic cell lines
☒	☐ Palaeontology
☐	☒ Animals and other organisms
☒	☐ Human research participants

Methods

n/a	Involved in the study
☒	☐ ChIP-seq
☐	☒ Flow cytometry
☒	☐ MRI-based neuroimaging

Unique biological materials

Policy information about availability of materials

Obtaining unique materials	All materials used are commercially available or made from commercially available materials (this applies to the nanoparticles). A detailed description of all the steps necessary to produce the nanoparticles is available in Methods.

Antibodies

Antibodies used	Information for the antibodies is listed as follows: fluorochrome; target; catalog #; supplier; clone; dilution FITC; CD34; 553733; BD; RAM34; 1:100 FITC; CD45.2; 553772; BD; 104; 1:100 FITC; Ly6c; 553104; BD; AL 21; 1:100 FITC; Ly6g; 127606; BioLegend; 1A8; 1:100 PE; B220; 103208; BioLegend; RA3-6B2; 1:100 PE; CD31; 102508; BioLegend; MEC13.3; 1:100 PE; CD90.2; 140308; BioLegend; 53-2,1; 1:100 PE; NK-1.1; 108708; BioLegend; PK136; 1:100

PE; Sca1; 12-5981-82; eBioscience; D7; 1:100
PE; Ter119; 553673; BD; TER-119; 1:100
PE; CD51; 104106; BioLegend; RMV-7; 1:50
PerCP5.5; CD41; 133918; BioLegend; MWReg30 ; 1:100
PerCP5.5; CX3CR1; 149010; BioLegend; SA011F11; 1:100
PE-Cy7; F4/80; 123114; BioLegend; BM8; 1:100
PE-Cy7; Sca1; 558162; BD; D7; 1:100
BV421; CD115; 135513; BioLegend; AFS98; 1:100
PacBlue; CD45.1; 110722; BioLegend; A20; 1:100
Aqua live cell; L34966; invitrogen; not applicable; 1:50
BV605; CD19; 115540; BioLegend; 6D5; 1:100
BV605; CD45.2; 563051; BD; 104; 1:100
BV605; CD140a; 135916; BioLegend; APA5; 1:100
BV605; ckit; 563146; BD; 2B8; 1:100
BV605; Ter119; 116239; BioLegend; TER-119; 1:100
Biotin; CD3epsilon; 100304; BioLegend; 145-2C11; 1:200
Biotin; CD4; 100404; BioLegend; GK1.5; 1:200
Biotin; CD8a; 100704; BioLegend; 53-6.7; 1:200
Biotin; CD90.2; 105304; BioLegend; 30-H12; 1:200
Biotin; CD19; 115504; BioLegend; 6D5; 1:200
Biotin; B220; 103204; BioLegend; RA3-6B2; 1:200
Biotin; CD11b; 101204; BioLegend; M1/70; 1:200
Biotin; CD11c; 117304; BioLegend; N418; 1:200
Biotin; GR1; 108404; BioLegend; RB6-8C5; 1:200
Biotin; Ter119; 116204; BioLegend; TER-119; 1:200
Biotin; NK-1.1; 108704; BioLegend; PK136; 1:200
Fc block; CD16/32; 553142; BD; 2.4G2; 1:100
BV711; CD16/32; 101337; BioLegend; 93; 1:100
BV711; CD45; 103147; BioLegend; 30-F11; 1:100
APC; Ly6g; 127614; BioLegend; 1A8; 1:100
AF647; CD11b; BioLegend; M1/70; 1:100
AF700; NK-1.1; 108730; BioLegend; PK136; 1:100
APC-Cy7; CD11b; 101218; BioLegend; M1/70; 1:100
APC-Cy7; Ter119; 560509; BD; TER-119; 1:100
APC-Cy7; CD45.2; 560694BD; 104; 1:100
APC/Fire; CD11b; 101262; BioLegend; M1/70; 10 mg/kg

Validation

All antibodies have been validated by the manufacturers for the applications used. The gating strategies used for identifying cell populations in this manuscript have been used and published by our group and others before.

CD34: Validated for use in mice and as a stem cell marker https://www.bdbiosciences.com/us/applications/research/stem-cell-research/cancer-research/mouse/fitc-rat-anti-mouse-cd34-ram34/p/553733 and is widely used for this application https://dx.doi.org/10.1016%2Fj.stem.2015.04.008
CD45: Validated for use in mice and as a leukocyte marker https://www.bdbiosciences.com/us/applications/research/stem-cell-research/cancer-research/mouse/fitc-mouse-anti-mouse-cd452-104/p/553772 and is widely used for this application https://dx.doi.org/10.1161%2FCIRCRESAHA.115.303567
Ly6c: Validated for use in mice and as a leukocyte marker https://www.bdbiosciences.com/us/reagents/research/antibodies-buffers/immunology-reagents/anti-mouse-antibodies/cell-surface-antigens/fitc-rat-anti-mouse-ly-6c-al-21/p/553104 and is widely used for this application https://dx.doi.org/10.1161%2FCIRCRESAHA.115.303567
B220: Validated for use in mice and as a leukocyte marker https://www.biolegend.com/en-us/products/pe-anti-mouse-human-cd45r-b220-antibody-447 and is widely used for this application https://dx.doi.org/10.1161%2FCIRCRESAHA.115.303567
CD31: Validated for use in mice and as a endothelial cell marker https://www.biolegend.com/en-us/products/pe-anti-mouse-cd31-antibody-379 and is widely used for this application https://dx.doi.org/10.1084%2Fjem.20070885
CD90.2: Validated for use in mice and as a leukocyte marker https://www.biolegend.com/fr-ch/products/pe-anti-mouse-cd90-2-thy-1-2-antibody-6867 and is widely used for this application https://dx.doi.org/10.1161%2FCIRCRESAHA.115.303567
NK-1.1: Validated for use in mice and as a leukocyte marker https://www.biolegend.com/en-us/products/pe-anti-mouse-nk-1-1-antibody-431 and is widely used for this application https://dx.doi.org/10.1161%2FCIRCRESAHA.115.303567
Sca1: Validated for use in mice and as a leukocyte and endothelial cell marker https://www.thermofisher.com/antibody/product/Ly-6A-E-Sca-1-Antibody-clone-D7-Monoclonal/12-5981-82 and is widely used for these applications https://dx.doi.org/10.1084%2Fjem.20070885 and https://dx.doi.org/10.1161%2FCIRCRESAHA.115.303567
Ter119: Validated for use in mice and as a red blood cell marker https://www.bdbiosciences.com/eu/applications/research/stem-cell-research/mesoderm-markers/mouse/pe-rat-anti-mouse-ter-119erythroid-cells-ter-119/p/553673 and is widely used for this application https://dx.doi.org/10.1161%2FCIRCRESAHA.115.303567
CD41: Validated for use in mice and as a stem cell marker https://www.biolegend.com/en-us/products/percp-cyanine5-5-anti-mouse-cd41-antibody-9696 and is widely used for this application https://dx.doi.org/10.1016%2Fj.stem.2015.04.008
CD51: Validated for use in mice https://www.biolegend.com/en-us/products/pe-anti-mouse-cd51-antibody-488 and used as an osteblast marker https://dx.doi.org/10.1038/nm.3589.
CX3CR1: Validated for use in mice and as a leukocyte marker https://www.biolegend.com/en-us/products/percp-cyanine5-5-anti-mouse-cx3cr1-antibody-10461 and is widely used for this application https://dx.doi.org/10.1161%2FCIRCRESAHA.115.303567
F4/80: Validated for use in mice and as a leukocyte marker https://www.biolegend.com/en-us/products/pe-cyanine7-anti-mouse-f4-80-antibody-4070 and is widely used for this application https://dx.doi.org/10.1161%2FCIRCRESAHA.115.303567
CD115: Validated for use in mice and as a leukocyte marker https://www.biolegend.com/en-us/products/brilliant-violet-421-anti-mouse-cd115-csf-1r-antibody-8971 and is widely used for this application https://dx.doi.org/10.1161%2FCIRCRESAHA.115.303567

CD19: Validated for use in mice and as a leukocyte marker https://www.biolegend.com/en-us/search-results/brilliant-violet-605-anti-mouse-cd19-antibody-7645 and is widely used for this application https://dx.doi.org/10.1161%2FCIRCRESAHA.115.303567

ckit: Validated for use in mice and as a stem cell marker https://www.bdbiosciences.com/us/applications/research/stem-cell-research/cancer-research/mouse/bv605-rat-anti-mouse-cd117-2b8/p/563146 and is widely used for this application https://dx.doi.org/10.1016%2Fj.stem.2015.04.008

CD3epsilon: Validated for use in mice and as a leukocyte marker https://www.biolegend.com/en-us/products/biotin-anti-mouse-cd3epsilon-antibody-22 and is widely used for this application https://dx.doi.org/10.1161%2FCIRCRESAHA.115.303567

CD4: Validated for use in mice and as a leukocyte marker https://www.biolegend.com/en-us/products/biotin-anti-mouse-cd4-antibody-247 and is widely used for this application https://dx.doi.org/10.1161%2FCIRCRESAHA.115.303567

CD8a: Validated for use in mice and as a leukocyte marker https://www.biolegend.com/en-us/products/biotin-anti-mouse-cd8a-antibody-152 and is widely used for this application https://dx.doi.org/10.1161%2FCIRCRESAHA.115.303567

CD11b: Validated for use in mice and as a leukocyte marker https://www.biolegend.com/en-us/products/biotin-anti-mouse-human-cd11b-antibody-346 and is widely used for this application https://dx.doi.org/10.1161%2FCIRCRESAHA.115.303567

CD11c: Validated for use in mice and as a leukocyte marker https://www.biolegend.com/en-us/products/biotin-anti-mouse-cd11c-antibody-1814 and is widely used for this application https://dx.doi.org/10.1161%2FCIRCRESAHA.115.303567

GR1: Validated for use in mice and as a leukocyte marker https://www.biolegend.com/en-us/products/biotin-anti-mouse-ly-6g-ly-6c-gr-1-antibody-457 and is widely used for this application https://dx.doi.org/10.1161%2FCIRCRESAHA.115.303567

CD16/32: Validated for use in mice and as a stem cell marker https://www.bdbiosciences.com/us/applications/research/b-cell-research/surface-markers/mouse/purified-rat-anti-mouse-cd16cd32-mouse-bd-fc-block-24g2/p/553142 and is widely used for this application https://dx.doi.org/10.1016%2Fj.stem.2015.04.008

Ly6g: Validated for use in mice and as a leukocyte marker https://www.biolegend.com/en-us/products/apc-anti-mouse-ly-6g-antibody-6115 and is widely used for this application https://dx.doi.org/10.1161%2FCIRCRESAHA.115.303567

Eukaryotic cell lines

Policy information about cell lines

Cell line source(s)	bEnd.3 (spelled BEND3 as well); manufacturer ATCC; catalog # CRL-2299
Authentication	The authentication was provided by the manufacturer.
Mycoplasma contamination	Mycoplasma free cells were purchased. No further testing for mycoplasma was done.
Commonly misidentified lines (See ICLAC register)	No commonly misidentified cell lines were used.

Animals and other organisms

Policy information about studies involving animals; ARRIVE guidelines recommended for reporting animal research

Laboratory animals	C57BL/6J(Jackson Laboratory, stock # 000664), B6.129P-Cx3cr1tm1Litt/J (Jackson Laboratory, stock # 005582), B6.SJLPtprcaPepcb/BoyJ (Jackson Laboratory, stock # 002014) mice were used at 11 to 13 weeks of age. To receive hemizygous B6.129P-Cx3cr1tm1Litt/J (Jackson Laboratory, stock # 002052) mice, homozygous mice were crossed with C57BL/6J mice. B6.129P2-Apoetm1Unc/J were started on high fat diet at 8 weeks of age. Mice of both sexes were used.
Wild animals	The study did not involve wild animals.
Field-collected samples	The study did not involve samples collected from the field.

Flow Cytometry

Plots

Confirm that:

☒ The axis labels state the marker and fluorochrome used (e.g. CD4-FITC).

☒ The axis scales are clearly visible. Include numbers along axes only for bottom left plot of group (a 'group' is an analysis of identical markers).

☒ All plots are contour plots with outliers or pseudocolor plots.

☒ A numerical value for number of cells or percentage (with statistics) is provided.

Methodology

Sample preparation	Single-cell suspensions were obtained from peripheral blood, bone marrow, aorta and lung. Briefly, blood was collected by eye bleeding using heparinised capillaries or, if larger volumes were needed, by cardiac puncture and the addition of 50 mmol/L EDTA. Red-blood-cell lysis was achieved by adding 1x red-blood-cell lysis buffer (Biolegend) for 2 minutes. After blood collection, mice were perfused through the left ventricle with 30 mL ice-cold PBS. Bone marrow was harvested by flushing femurs in PBS with 0.5% bovine serum albumin (BSA) for leukocyte and HSPC staining or with HBSS containing 2% FBS, 2 mg/ml disease 2 and 1 mg/ml collagenase IV and incubated with gentle agitation for 30 minutes at 37°C for endothelial cells. Lungs were excised and minced with a fine scissor before digestion in DMEM w/o phenol red containing 2% FBS, 2 mg/ml dispase 2, 5 mg/ml collagenase I (Worthington) and 1 mg/ml DNase I (Sigma) at 37°C and 125 revolutions for 20 minutes. Tissues were then plunged thorough

40-µm nylon mesh (BD Falcon), washed and centrifuged (8 minutes; 300g; 4°C). The obtained single-cell suspensions were stained at 4°C for 30 minutes and afterwards washed, centrifuged and resuspended.

Instrument

LSR II flow cytometer with BD FACSDiva software. For cell sorting the populations were defined as described and sorted using a FACSAria II cell sorter.

Software

FlowJo V9

Cell population abundance

For qPCR experiments at least 10.000 cells were sorted. Purity for endothelial cells was confirmed by a second sorting step, PCR and microscopy.

Gating strategy

Monocytes were identified as CD90- CD19- NK1.1- Ly-6G- D45.2+ CD11bhighCD115+ F4/80low and separated into Ly-6Clow and a Ly-6Chigh populations. Neutrophils were identified as CD90- CD19- NK1.1- D45.2+ CD11bhigh Ly-6G+. Blood and bone marrow LSK were identified as (B220 CD3e CD4 CD8a CD11b CD11c CD19 CD90.2 GR1 IL7Ra NK1.1 Ter119)- c-kit+ Sca-1+, LKs as (B220 CD3e CD4 CD8a CD11b CD11c CD19 CD90.2 GR1 NK1.1 Ter119)- c-kit+ Sca-1- and subdivided into CMP, MEP and GMP by their CD16/32 and CD34 expression. Bone-marrow and lung endothelial cells were gated as CD45.2- CD41- Ter119- CD31+ Sca-1+ and Ter119- CD45+ CD31+, respectively.

☒ Tick this box to confirm that a figure exemplifying the gating strategy is provided in the Supplementary Information.